9-1-2012

Three-dimensional quantification and visualization of vascular networks in engineered tissues

Mohammed Yousefhussien

Three-dimensional Quantification and Visualization of Vascular Networks in Engineered Tissues

by

Mohammed Assad Yousefhussien

A Thesis Submitted in Partial Fulfillment of the Requirements for the Degree of Master of Science in Electrical and Microelectronic Engineering

Supervised by

Prof. Maria Helguera
Chester F. Carlson
Center for Imaging Science
Rochester Institute of Technology
Rochester, NY
September 2012

Approved By:

Prof. Maria Helguera
Primary Advisor – R.I.T. Center of Imaging Science

Prof. Eli Saber
Secondary Advisor – R.I.T. Dept. of Electrical and Microelectronic Engineering

---

Prof. Dorin Patru
Secondary Advisor – R.I.T. Dept. of Electrical and Microelectronic Engineering

---

Prof. Sohail A. Dianat
Dept. Head – R.I.T. Dept. of Electrical and Microelectronic Engineering

Dedication

To my father Dr. Assad Yousef M.D.

To my mother Inaam

To my brother & sister Shadi & Haneen

To my wife & daughter Safaa & Rafeef

To IIE & AMIDEAST

Acknowledgements

It would not have been possible to write this Master thesis without the help and support of the kind people around me. Above all, I would like to thank my parents, brother, and sister who have given me their support throughout the two years I spent them far from them, which my mere expression of thanks likewise does not suffice. This work wouldn't have been possible without the great support and patience at all times from my wife and my daughter Safaa and Rafeef.

My sincere thanks go to my second advisor, Dr. Maria Helguera, for the good advice, support and friendship of her, which has been invaluable on both an academic and a personal level, for which I am extremely grateful. I would like to acknowledge the help and the academic support that Dr. Nathan Cahill gave me whenever I needed an answer to any image processing problem. My deepest gratitude to my friends Dr. Mustafa Jaber, Muhannad Darnasser, Kunal Vaidya, Sreenath Vantaram, Abdul Haleem Syed, and Ye Lu for being there for me.

I also thank the people at the Department of Biomedical Engineering - University of Rochester for providing me with the image data and their continuous support and feedback for this work.

Finally, I would like to extend my pleasure to thank the person who always supported, encouraged, and guided me throughout my studies alongside this work, where it was a great pleasure being his student and work with him. Thank you Dr. Eli Saber for all what you gave me.

Mohammed Yousefhussien

Abstract

Three-dimensional textural and volumetric image analysis holds great potential in understanding the image data produced by multi-photon microscopy. In this thesis, a tool that provides quantitative textural and morphometric analyzes of vasculature in engineered tissues, alongside with a fast three-dimensional volume rendering is proposed. The investigated 3D artificial tissues consist of Human Umbilical Vein Endothelial Cells (HUVEC) embedded in collagen exposed to two regimes of ultrasound standing wave fields under different pressure conditions. Textural features were evaluated over the extracted connected region in our samples using the normalized Gray Level Co-occurrence Matrix (GLCM) combined with Gray-Level Run Length Matrix (GLRLM) analysis. To minimize the error resulting from any possible volumetric rotation and to provide a comprehensive textural analysis, an averaged version of nine GLCM and GLRLM orientations is used. To evaluate volumetric features, parameters such as volume run length and percentage volume were utilized. The z-projection versions of the samples were used to estimate the tortuosity of the vessels, as well as, to measure the length and the angle of the branches. We utilized a three-dimensional volume rendering technique named MATVTK (derived from MATLAB and VTK) and runs under MATLAB that shows a great improvement on the processing time to reconstruct our volumes compared to MATLAB built-in functions. Results show that our analysis is able to differentiate among the exposed samples, due to morphological changes induced by the ultrasound standing wave fields. Furthermore, we demonstrate that providing more textural parameters than what is currently being reported in the literature, enhances the quantitative understanding of the heterogeneity of artificial tissues.

Table of Contents

List of Figures

List of Tables

Chapter 1 INTRODUCTION

1.1 OBJECTIVES AND MOTIVATIONS

Microbiological three-dimensional image analysis is rapidly becoming more interesting to researchers, due to the huge image data produced by modern scanning tools such as Mirco-CT, Confocal microscope, and Multi-photon microscope. This type of analysis provides microbiological scientists with a solid ground to support their qualitative observations using parametric quantification. The need for quantification algorithms that efficiently provide a comprehensive three-dimensional analysis, by quantifying the biological heterogeneity and the morphological characteristics while providing a three-dimensional volume reconstruction all in one package, laid the foundation of this work to provide a simple and easy-to-use Graphical User Interface (GUI) that assists the scientists working in the field of artificial tissue engineering in quantifying their observations.

1.2 LITERATURE REVIEW

Qualitative image analysis usually tries to differentiate between sets of experiments by examining the image data manually and using a single image at a time without quantitative parameters to support their observations. Many methodologies have been proposed in the past to provide a solution to this problem. Some algorithms tackled a single quantification problem such as counting cells or tortuosity. Other algorithms provided either a full textural or volumetric quantification alongside with a reconstruction technique, while few of them combined both quantification techniques.

The authors in [1] developed a two-dimensional automatic counting of cell colonies algorithm that was divided into two stages. The first stage was developed to target cell types that have a good contrast with respect to the background. Methods such as background subtraction, edge detection, and morphological operations were used in this stage. The second stage targeted the ill-defined or fuzzy colonies with low contrast by using the edge information with a compact Hough transform to enhance circular shapes while suppressing straight lines. However, the algorithm didn't provide any quantification features beyond the counting algorithm. In [2], the authors developed a two stage automatic segmentation algorithm to extract and quantify three-dimensional mouse embryonic cell images produced by a fluorescence microscope. Prior to segmentation, a two-dimensional preprocessing operations using top-hat transform, automatic thresholding, masking, and median filtering were applied to eliminate the effect of bright condensed regions. The first step in the segmentation process involved a three-dimensional adaptive thresholding mechanism to extract complete cell clusters. A three-dimensional Euclidean distance and watershed segmentation were then applied to subdivide cellular regions. In the second step, the algorithm utilized a three-dimensional level set algorithm operating on the Laplacian images to determine fuzzy borders that weren't detected by thresholding. The quantification measurements were performed semi-automatically, however, the reported features only included nuclei volume and distances to the nuclear centers and peripheries.

In [3], Textural features were included alongside with a single morphological measurement. The study used co-occurrence matrix calculation [4] to identify between two types of abnormal prostatic tissues, while the area measurement of large lumens was

utilized to classify normal tissues. Even though this study doesn't provide the biological meaning of the textural features, it shows that textural techniques are useful to discriminate between pathological status of tissues. On the other hand, the algorithm didn't provide any structural information.

For a full volumetric quantification [5,6], a three-dimensional algorithm to quantify microvascular network of human cerebral cortex was introduced in [5]. The images were captured using confocal microscope, and a preprocessing stage using two-dimensional median filtering was applied. The algorithm provided comprehensive three-dimensional quantification parameters such as microvessel density, orientations, distances, number of segments, lengths, volume. However in [6], the algorithm included tortuosity as a measurement for complex vascular networks, neither algorithm provided any textural quantification. The work in [7,9] provided a full and complete quantification by utilizing both textural and volumetric measurements. In [7], the developed algorithm implemented a two-dimensional quantification of biofilm images. It utilized three parameters evaluated using Gray Level Concurrence Matrix (GLCM) to quantify textural information, while two-dimensional areal features such as porosity, fractal dimension, and run length were used to quantify structural information. The authors in [8] decided to take the quantification to a further step. Their developed algorithm didn't include textural analysis, but it expanded the structural parameters to three-dimensional volumetric parameters while adding more measurements. As a full improvement over [7,8], the algorithm developed in [9] included a three-dimensional textural analysis alongside a three-dimensional volumetric analysis. The developed software expanded the GLCM to a third dimension by evaluating the dependence matrices in the three main orientations.

Besides evaluating four volumetric features, the authors in [10] introduced a three-dimensional reconstruction algorithm for cell nuclei. Their algorithm proposed surface rendering and volume rendering methods written in C++ language and OpenGL. In volume rendering, the algorithm separated volumetric data set into structural units by three-dimensional labeling. After adding coordinates, intensities, and gradient vectors information to the structural units, a bilinear interpolation scheme was utilized to generate new values between the actual voxels. By using ray casting graphical algorithm and assigning different colors and opacities to the voxels, the algorithm enabled three-dimensional view from two-dimensional stacks of images, while no textural quantification were reported in this study. Other techniques include registration before the reconstruction as in [11]. The reported images show that the algorithm displayed a solid three-dimensional object that enabled viewing front faces of the rendered volume only. However, to view dept, the authors provided a displaying method that utilizes x, y, z plane images to intersect at the desired point of interest.

Other techniques utilize the information such as diameter, angle, and length extracted from volumetric analysis to reconstruct three-dimensional objects by assuming cylindrical shapes that vary according to the previously mention features [12]. The reconstruction method wasn't reported in the previous reference. For more information about other techniques, the reader is referred to [13,14,15], where in [15] a recent full three-dimensional reconstruction tool is presented without any quantification features.

1.3 CONTRIBUTION

Due to the novelty of the microbiological engineering technique used to induce different vasculature networks, to the best of our knowledge, we believe there is no preliminary work on quantitative image analysis and three-dimensional visualization of Ultrasound Standing Wave Field (USWF) induced vasculature networks. In this work, we present an algorithm that quantifies three-dimensional vasculature networks in engineered tissues. Our algorithm includes two different three-dimensional textural analyses evaluated from nine directions as an improvement on the algorithm presented in [9] to quantify the heterogeneity of our induced patterns. The algorithm starts with an enhancement process followed by a simple segmentation using threshold technique to eliminate background noise and uneven illumination. A three-dimensional connected component analysis is applied in the following step to extract our volume of interest. As a quantification step, our textural analysis utilized four statistical features computed using (GLCM) method which incorporates voxels intensives to describe texture, as well as Gray Level Run Length Matrix (GLRLM) which adds structural information by using run length technique. Combining both methods makes the textural quantification more informative, where each technique explains the behavior of the features from the other one. Also, we provide selected volumetric parameters computed in nine directions. Finally, we introduce a very fast volume reconstruction through MATLAB environment with the instructions on how to setup and establish this feature for future use to provide a complete tool that helps the scientists in quantifying their observations and enables them to differentiate between their experiments.

1.4 THESIS OUTLINE

This work is organized as follows. In Chapter 2 a background about tissue engineering and the techniques used to create each tissue as well as the experimental data are presented in this chapter. The proposed algorithm including the preprocessing steps and the volume quantification in terms of textural, volumetric, tortuosity, length, and angle measurements is presented in Chapter 3. Chapter 3 also shows the three-dimensional volume rendering using the new rendering technique through linking MATLAB environment with the visualization tool VTK, and describes the developed GUI and its functions. In Chapter 4, the results are discussed by comparing the quantitative analysis between the experimental data evaluated using the developed tool, and show that our analysis supports the qualitative analysis. Finally, Chapter 5 draws conclusions and proposes future work.

Chapter 2 BACKGROUND

Tissue engineering is the study of recreating or replacing diseased or damaged organs and tissue by growing connective tissue using cells extracted from the body. This technique allows newly developed tissues to be implanted and grown inside the donor's body without immunological rejection. In a simple description of fabricating tissues and organs, the cells are seeded within an appropriate microenvironment that promotes cell communication and growth. When the cells find the growth factors, they start to multiply in number and grow into a three-dimensional tissue. Once the tissue is ready, it is implanted in the body and eventually the cells start their intended function. To keep the implanted tissue functioning, blood vessels start to connect to the new tissue for nourishment. For such a process to achieve its success, an appropriate microenvironment that promotes tissue regeneration, as well as a rapid development of vascular networks is needed.

To prepare the appropriate microenvironment, two different techniques were reported to organize cells in complex patterns. In the first approach, pre-designed micro-patterns are used to direct the cells to create complex structures, while in the second approach an external force is applied to direct the cells to a certain location. Different forces such as fluidic, magnetic, electro kinetic or optical are reported in the literature. On the other hand, to vascularize engineered tissue, two general strategies are under development. The first strategy depends on the natural growth of the body's blood vessels to attach with the implanted tissue in order to form a vascular network inside it. Such a process is reported to be slow, which can compromise tissue viability. As an improvement on the previous method, the second strategy depends on the formation of

the vascular network within the engineered tissue prior to the implantation to minimize the perfusion time after the implantation.

In this work, we utilize image processing techniques to quantitatively characterize vascular networks induced by the recent novel application, which utilized (USWF) to vascularize engineered tissues, as reported in [16,17,18].

2.1 EXPERIMENTAL DATA

Ultrasound Standing Wave Fields (USWF) has been demonstrated to non-invasively control the spatial distributions of cells within three-dimensional, collagen-based engineered tissues. Ultrasound-induced alignment of mouse embryonic myofibroblasts in collagen gels increases cell contractility and cell-mediated extracellular matrix reorganization. Noninvasive organization of endothelial cells within collagen gels accelerates the formation of capillary sprouts that mature into branching networks throughout the three-dimensional hydrogel. Both the rate of formation and morphology of the resultant vascular network are dependent upon the ultrasound field parameters used to produce the cellular alignment. Multi-photon microscopy imaging techniques are employed to visualize these branching networks, as shown in Figure 1.

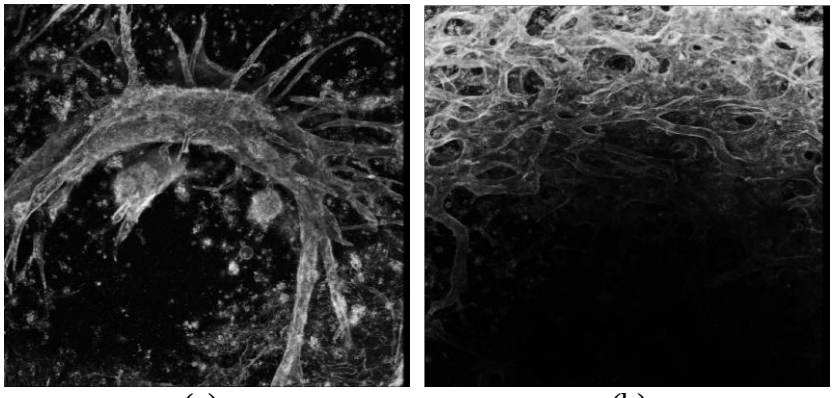

(a) (b)

Figure 1. (a) 2 MHz - 0.2 MPa image, (b) 1 MHz - 0.1 MPa image

It was observed that at 1MHz, changing the pressure amplitude from low to high resulted in loosely aggregated cell bands at low pressure, while dense cell bands were formed at high pressure. Based on these differences in initial cell band density, we observed that the resulting vascular structure differed. Loosely aggregated cell bands led to the formation of dense vascular network. On the other hand, densely packed cell bands formed into sprouting networks with a vascular tree-like morphology. In 2MHz, the (USWF) pattern differs and the cell bands that are formed are closer together than those formed at 1 MHz. However, the low and high pressure amplitudes chosen for the 2 MHz exposures resulted in similar initial cell band density than the 1 MHz pressures used. So the low pressure of 0.08 MPa results in loosely aggregated cell bands while the high pressure of 0.2 MPa results in densely packed cell bands. Human Umbilical Vein Endothelial Cells (HUVEC) were suspended in an unpolymerized type I collagen solution and were exposed to either a 1 or 2 MHz (USWF) at various (USWF) peak positive pressure amplitudes (1 MHz - sham, 0.1 MPa, 0.3 MPa; 2 MHz - sham, 0.08 MPa, 0.2 MPa). Collagen solutions were allowed to polymerize during the 15 min exposure period to effectively maintain (USWF) induced cell alignment after removal of the sound field. Exposure of (HUVEC) at the stated pressures resulted in either a homogeneous cell distribution (sham exposure), loosely aggregated cell bands (0.1 MPa at 1 MHz and 0.08 MPa at 2 MHz), or densely packed cell bands (0.3 MPa at 1 MHz and 0.2 MPa at 2 MHz). Samples were incubated for 10 days post (USWF) exposure and then fixed in 4% paraformaldehyde. These experiments were repeated three times for each condition. Standard immunofluorescence protocols were used to label (HUVEC) membranes with an antibody directed against (CD31) and cell nuclei were identified by

staining with (DAPI). Samples were then examined using multi-photon immunofluorescence microscopy to noninvasively scan through the three-dimensional volume of the engineered tissue. Images were collected in the z-direction in 1 μm step size generating stacks of 300 to 400 images. The spatial dimensions of each voxel are 2.5 x 2.5 x 1 μm^3.

In this study, we utilize stacks of multi-photon microscopy images to develop three-dimensional textural and volumetric image analysis techniques to quantitatively characterize the structure of networks formed within various engineered tissues.

Chapter 3 PROPOSED ALGORITHM

To better understand, compare, and monitor the samples development, a three-dimensional image analysis to quantify the volume structure is needed. A preprocessing stage is required to enhance the stack of images before any further calculation. Figure 2 describes the entire process in terms of a flowchart.

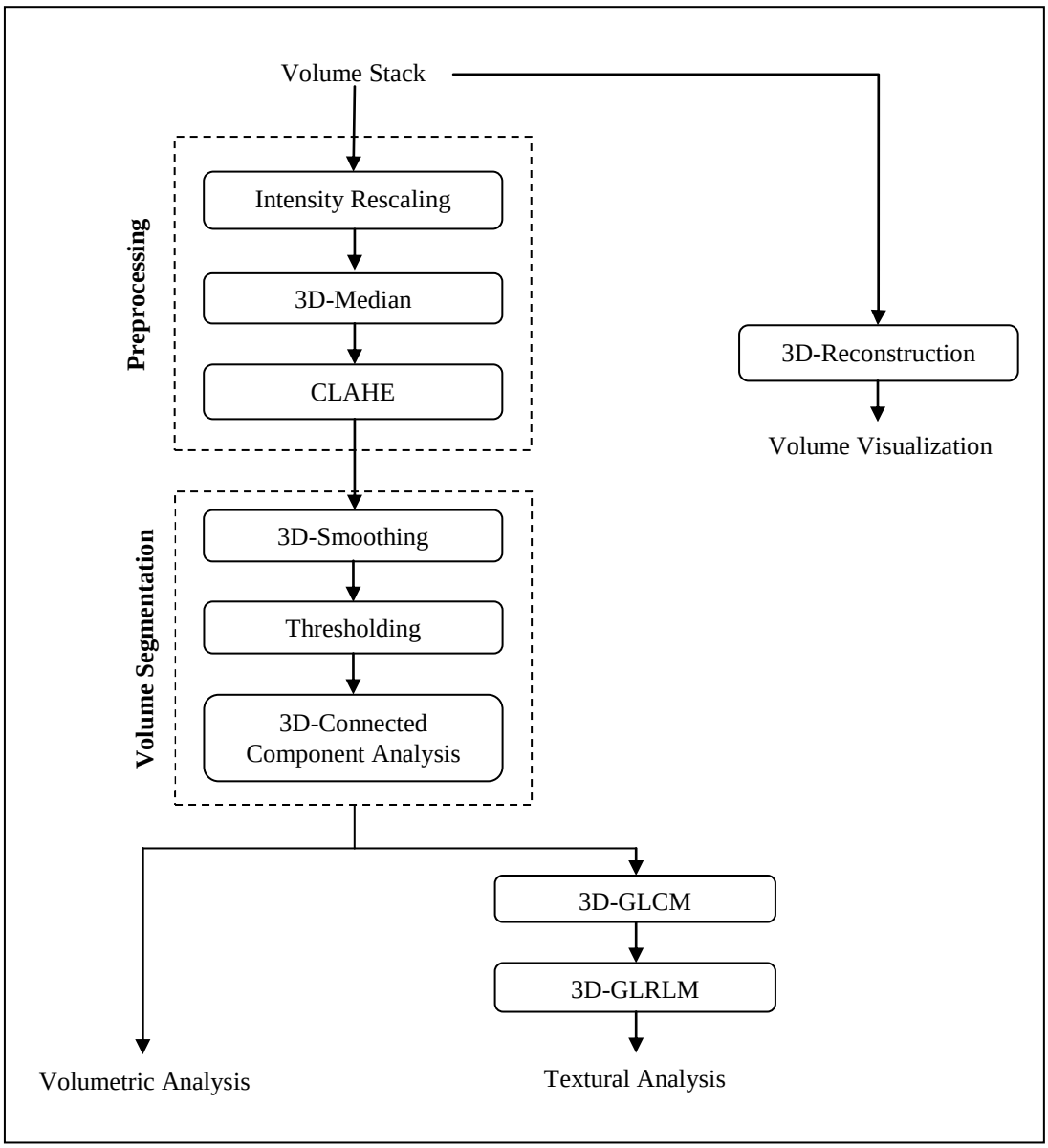

Figure 2. A block diagram that shows the proposed algorithm

3.1 Preprocessing

Multi-photon microscopy produces 16-bit depth images, however after close examination, three issues were identified. First, even though the images are stored in 16-bit depth, their gray level values never exceed the value of 4096, which means that the images, in fact, are 12-bit depth as shown in Figure 3 (b). To process and display the images without changing their intensity distribution, they were normalized by dividing each one by the maximum value.

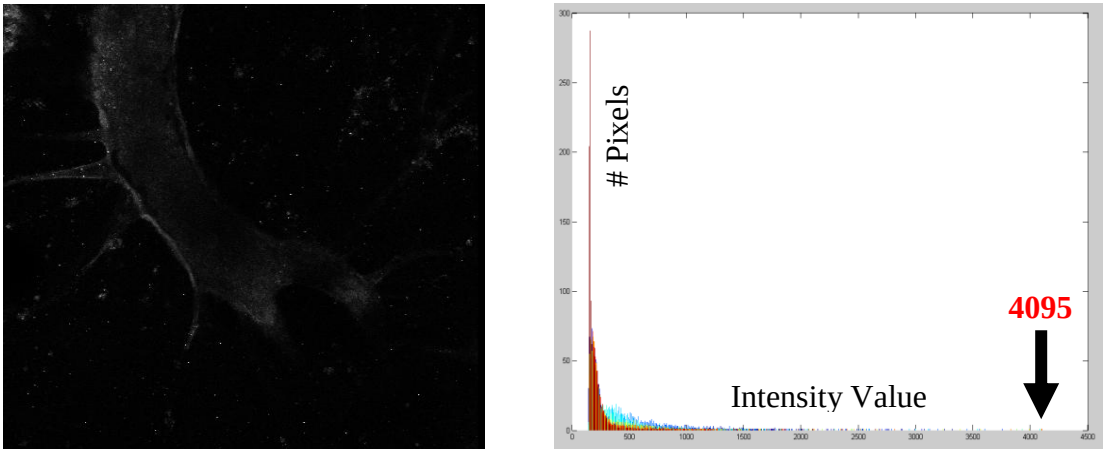

(a) (b)

Figure 3. (a) A single image of one sample , and (b) the corresponding histogram of the image in (a). The histogram shows a narrow distribution as well as the maximum gray level value which doesn't exceed 4095.

Second, the intensity distribution of the images follows a very narrow unimodal histogram centered at low intensity values as shown in Figure 3 (b). Such distribution produces poor, low-contrast images, which are difficult to deal with. To overcome this issue, a Contrast Limited Adaptive Histogram Equalization (CLAHE) was applied with a 7 x 7 pixels window size in order to enhance the contrast for better processing, while preventing the over amplification of noise that global or adaptive histogram equalization can produce in such cases. Histogram Equalization (HE) tries to transform the pixel

values of an image so that they occupy the full range of intensities regardless of the histogram distribution [19-20]. Assume $P_r(r_k)$ is the normalized histogram of a given image, where k=0,2,...,L-1 is the intensity level, and L is the number of gray levels. The goal of the process is to generate an image with equally likely intensity values. The normalized histogram serves as a Probability Density Function (PDF), where each single value refers to the probability of occurrence of each gray level in the image. To transform the random (PDF) of the image into a uniform distribution, an equalization transformation function is used as in Eq. (1)

$$S_k = T(r_k) = (L-1)\sum_{j=0}^{k} P_r(r_j) = (L-1)\sum_{j=0}^{k} \frac{n_j}{MN} \quad (1)$$

where S_k is the new distribution and $T(r_k)$ is the transformation function modeled as the Cumulative Distribution Function (CDF) of the original histogram. The constant *MN* is the number of pixels in the image, while n_j refers to the number of pixels in gray level *j*. Since (HE) applies the transformation over the entire histogram as a whole, a huge noise amplification is a natural result especially for narrow histogram distributions. Adaptive Histogram Equalization (AHE) has the advantage of being applied locally by dividing the image into small regions and performing (HE) on each single region separately or overlapping [19,20]. The results of the (AHE) hold great improvement in our images, but noise amplification still exist which produces unwanted regions at the segmentation step. In (CLAHE), the height of the histogram is clipped at a certain level, enforcing a maximum on the counts of the histogram that in return will limit the contrast enhancement and the noise amplification **[**21**]**. Then the clipped regions of the histogram are added uniformly to the rest of the distribution so that the entire input intensity is

mapped to the full output intensity range as described in Figure 4. Different results are shown in Figure 5 after further enhancement for displaying purpose.

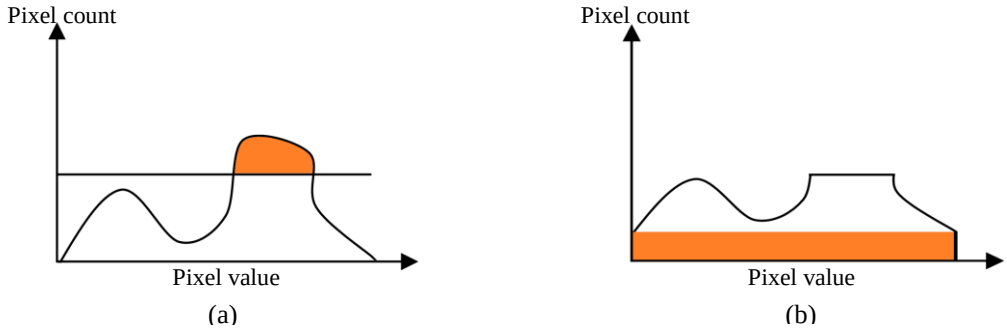

Figure 4. (a) The original histogram with the clipped region before redistribution, and (b) the clipped region is distributed uniformly throughout the histogram.

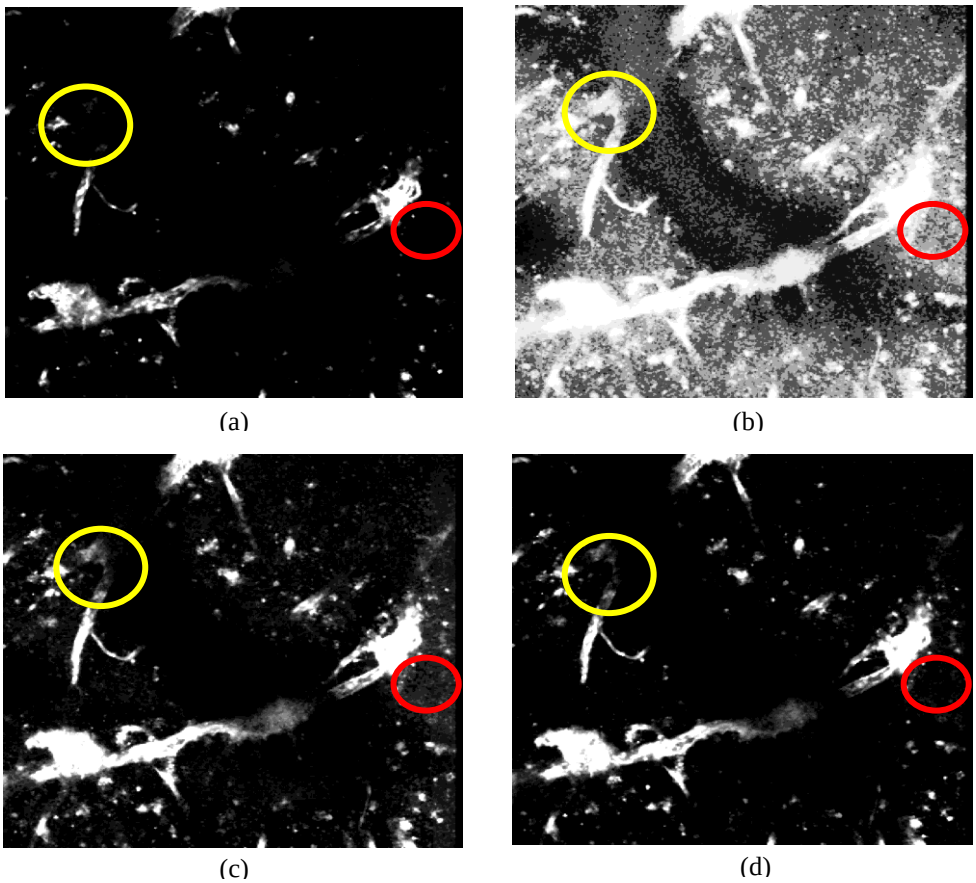

Figure 5. (a) The original image, (b) global histogram equalization, (c) adaptive histogram equalization, and (d) with Contrast Limited Adaptive Histogram Equalization. The red circles shows the level of noise in the same region, while the yellow circles shows the effect of preserving structural regions.

The third issue was due to the staining of the samples, where cellular debris is captured alongside the vasculature structure which affects the images with a salt and pepper-type noise. To remove such noise, we utilized a three-dimensional median filtering algorithm with a cube of 3 x 3 x 3 voxels as shown in Figure 6.

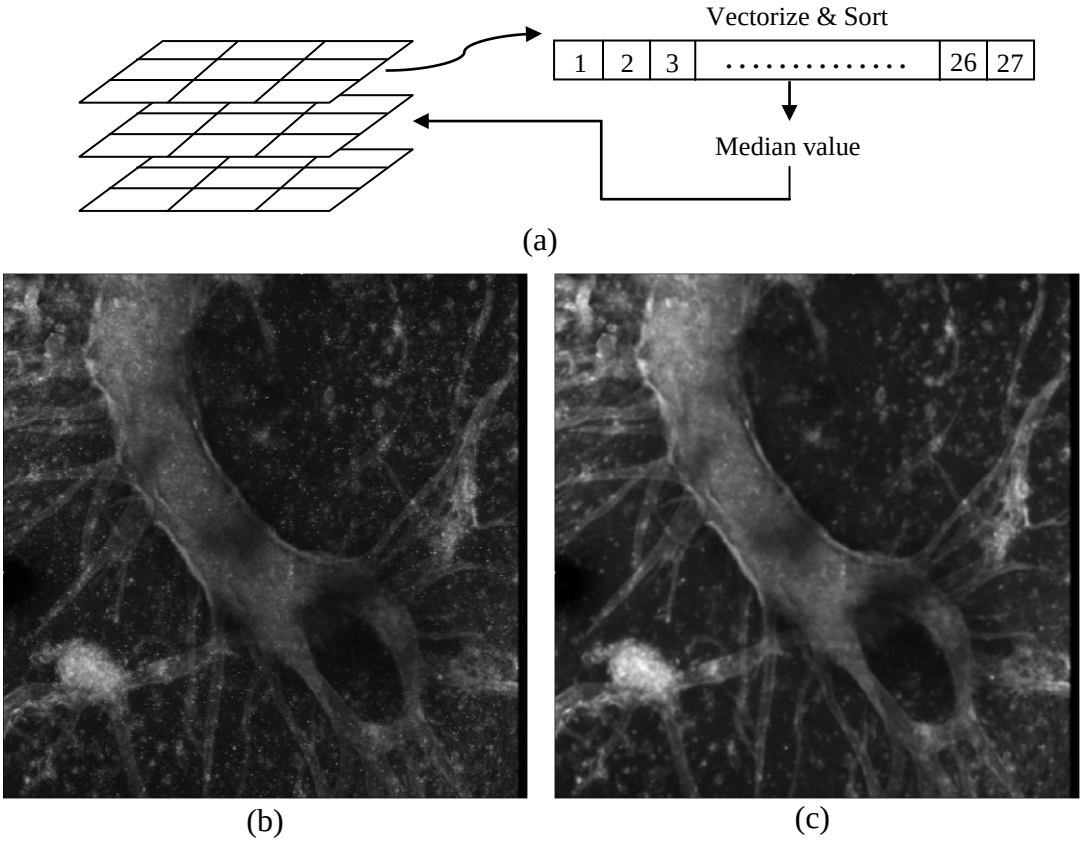

Figure 6. (a) The graph shows the process of the three-dimensional median filter, while (b) and (c) shows the z-projected version of the images before and after the filtering respectively.

Combining those preprocessing steps results in noise reduction while maintaining the high spatial frequency content in each image. It is important that the three steps mentioned above follow a certain order. At first we rescaled the intensities, then we applied median filtering, and at the end we performed the intensity enhancement using (CLAHE). Putting the median filtering before the (CLAHE) prevented the salt and pepper noise enhancement alongside the actual biological structure.

3.2 Volume Segmentation

To achieve accurate analysis, the effect of the uneven illumination needs to be eliminated from the background, which is produced due to the scanning process of the samples. On the other hand, all the relatively small objects that weren't removed by the three-dimensional median filter and don't contribute to the volume of interest need to be removed. In order to achieve this goal, two steps were applied. The first step aims to remove the background from each image, which will prevent the textural analysis from producing misleading results due to uneven illumination. This is done by thresholding each single image of the stack automatically using the mean value of each image. Other methods such as Otsu didn't work well due to the single peaked narrow intensity distribution of the images as shown in Figure 7.

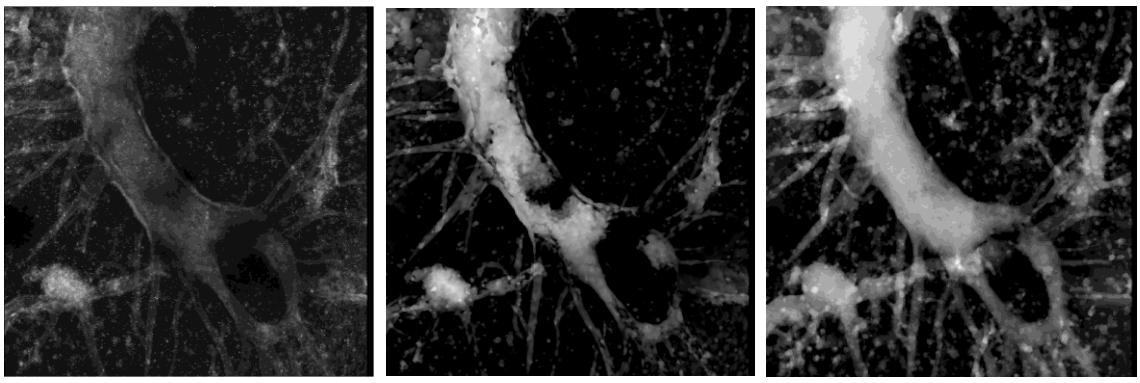

(a) (b) (c)

Figure 7. (a) The original image, (b) the result after Otsu thresholding, and (c) the result after the mean value thresholding.

However, an effect of over quantification might result due to small gaps or discontinuities that occur after thresholding. In order to reduce this effect, a three-dimensional smoothing filter is utilized before the thresholding step to connect such gaps between clusters. For more information about thresholding in tissue analysis, the reader is referred to [22], where different thresholding techniques for engineered tissue images have been

evaluated and discussed. The second step includes a three-dimensional connected component analysis, where a 26-connectivity was used to ensure all the neighbors of each voxel are covered. Any set of pixels which is not separated by a boundary is considered a connected component. In order to extract the connected regions in an image, a labeling step is required. Different segmentation algorithms ranging from simple thresholding to more advanced techniques such as region growing and K-means clustering are used before the labeling step. It is worth mentioning that advanced segmentation algorithms incorporate labeling within the segmentation algorithm when providing the final results. To label binary images, different gray level values starting from 1 to the number of the connected regions are assigned to each region. Different searching neighborhoods (4,8-connected neighborhood for two-dimensional images, and 6,18,26-connected neighborhood for three-dimensional volumes) are used for different connectivity options. Filtering the connected components by size enables further processing over the extracted regions. By choosing different connected volume sizes and visually inspecting the results, we found that the volume of interest always gets extracted by choosing the largest connected volume. This step will ensure a connectivity of the volume of interest, while removing other regions that may contribute as noise as shown in Figure 8.

3.3 Textural Quantification

We recognize texture when we look at different patterns, but it is difficult to define it. For our application we define texture analysis as the ability to differentiate between different pattern arrangements due to the existence of repetitive, random, or uniform properties. Texture analysis is used in different application such as texture

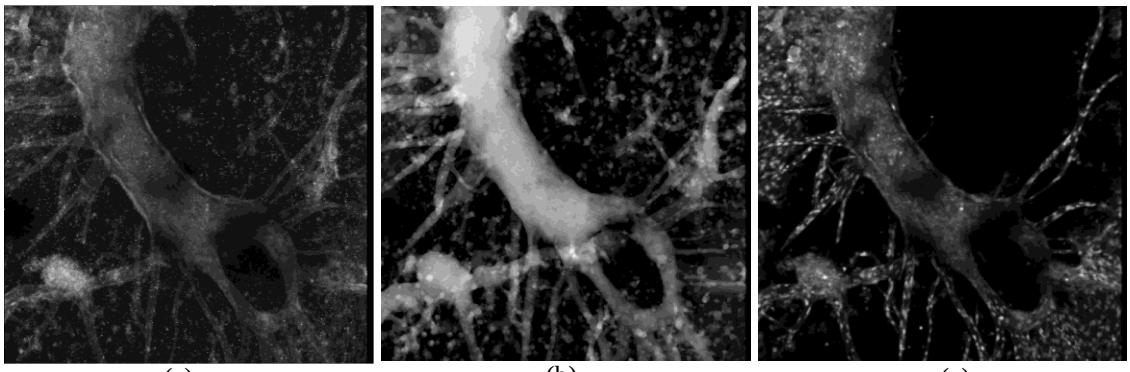

(a) (b) (c)

Figure 8. (a) The original image, (b) the result after thresholding, and (c) the result after extracting the largest connected region.

classification, where producing a classification map of the identified textural regions are required, and textural segmentation which divides the image into none overlapping regions according to their textural properties. Our textural analysis aims mainly to describe the textural changes that occur in different induced vascular networks when being exposed to different (USWF) settings more than a classification or a segmentation process. Textural features can be calculated by statistical methods, geometric methods, model based methods, or signal processing methods such as (GLCM), Voronoi Tessellation, Fractals, and Fourier transform respectively [23]. Since our work utilizes statistical methods, we should explain two types of statistical concepts:

i) *First-order statistics:* which measures a probability of observing gray levels at a randomly selected location in an image. This type of statistics doesn't incorporate pixel position or the effect of the neighboring pixels, but only depends on individual pixel value. Such statistics can be calculated from the histogram such as the average image intensity.

ii) *Second-order statistics:* which takes into account the likelihood of observing the gray level values in the neighborhood at different distances and orientations. In our

work we included two different textural analyses belonging to this group, since they incorporate pixel location, orientation, and neighboring pixels information.

3.3.1 Gray Level Co-occurrence Matrix (GLCM)

The Haralick (GLCM) [24] is one of the most popular methods that utilize pixel variation statistics in textural analysis. it uses a dependence matrix that represents the distribution of change in gray level values of neighboring pixels. To evaluate the dependence matrix, three different parameters should be pre-set in order to achieve the desired accuracy in determining the textural features as follow.

i) *Quantization Levels:* the size of the (GLCM) is dependent on the quantization level, since it is a square matrix with a dimension estimated by the maximum gray value in an image. When more levels are included in the calculation, an increase of the accuracy is achieved, however, the computational cost is increased as well and vice versa.

ii) *Displacement:* this parameter defines the neighboring pixels to be compared with the current pixel. Applying a large displacement value results is a (GLCM) that doesn't capture detailed texture, while the opposite is true as well.

iii) *Orientation:* it defines the direction in which the texture is being estimated. Since each pixel has eight neighboring pixels, eight orientation angles which are 0°, 45°, 90°, 135°, 180°, 225°, 270°, and 315° are defined. However, evaluating the texture in 0° or 180° will produce the same value for a textural feature. Since this is true for the rest of the orientations, this reduces the orientation angles into four directions. In [24] it was

recommended that one should estimate the textural features in all four directions in order to avoid rotational errors and to capture every possible textural information as well.

In our work, the previous parameters were chosen as follow: different quantization levels varying from 8 to 256 were tested for textural quantification, however huge differences in values were observed; therefore we used the quantization level of 256 for this analysis by utilizing uniform quantization. Levels higher than 256 were not used due to processing time. A displacement of value 1 was also chosen in order to capture the micro-scale textural changes that occur in the vascular network. Finally, since our samples are three-dimensional objects, we extended the orientations to cover nine directions in three planes as shown in Table 1.

Table 1. Different orientation angles in three planes.

Plane	**XY**				**YZ**			**XZ**	
Angle	0°	45°	90°	135°	45°	90°	135°	45°	135°

In [24], eight textural features can be evaluated from (GLCM), but in this application we chose four of them which can be interpreted into a physical meaning describing the textural changes in our samples. The four textural parameters were calculated over the largest connected volume as follow:

i) *Entropy (ENT)*

Entropy is a measurement of randomness and is defined by

$$ENT = -\sum_{i=0}^{N-1}\sum_{j=0}^{N-1} p(i, j) \cdot \log(\, p(i, j)) \tag{2}$$

where N is the number of gray levels in the image after quantization, $p(i, j)$ is the probability value in the (GLCM) at location (i, j). When the image is not uniform, the

(GLCM) will contain many elements of small values, which results in a very large entropy value. In other words, a random texture will result in higher entropy values, while a smoother texture will result in lower entropy values. In our case, the entropy can serve also as a complexity measurement, where a higher value refers to a more complex structure.

ii) *Energy (ENE)*

Energy is also called Angular Second Moment (ASM). This parameter was utilized as a measurement of cluster repetition and uniformity, and it is defined by

$$ENE = \sum_{i=0}^{N-1} \sum_{j=0}^{N-1} p^2(i, j) \tag{3}$$

For this parameter to reach its maximum value of 1, a few elements in the GLCM should be close to 1, while many elements should be close to 0. In other words, a higher energy value means more periodic and uniform clusters in the volume, while the ideal case happens when the volume has a constant intensity level where the energy value equals 1.

iii) *Contrast (CON)*

Contrast measures the difference between the highest and the lowest intensity values of contiguous pixels and it is defined by

$$CON = \sum_{i=0}^{N-1} \sum_{j=0}^{N-1} p(i, j) \cdot (i - j)^2 \tag{4}$$

where the values range between 0 and $(N-1)^2$. Higher contrast corresponds to busier texture and sharper, more frequent transitions between the gray levels.

iv) *Homogeneity (HOM)*

Homogeneity measures the similarity and the smoothness between the intensity values of neighboring pixels. It is defined by

$$HOM = \sum_{i=0}^{N-1}\sum_{j=0}^{N-1}\frac{p(i,j)}{1+(i-j)^2} \quad (5)$$

where higher homogeneity corresponds to smoother and more similar regions in the volume.

3.3.2 Gray Level Run Length Matrix (GLRLM)

Run length analysis captures the textural information in a specific direction. A run is defined as a group of consecutive pixels that have the same gray level value along a specific orientation. Fine texture tends to contain a higher number of short runs with similar intensities, while coarse texture has longer runs [25].

The run length matrix R is defined as follows: the elements R(i,j) refer to the number of runs with pixels of gray levels (i) and length of runs equal (j) along a certain orientation. The size of the matrix is M by N, where M is the number of the gray levels in the image, while N is the maximum possible run across the image. The following figure shows a simple example describing the calculation of a run length matrix.

Image

1	1	2	1
2	3	2	2
3	4	4	3
1	2	3	4

Run length **0°**

0°	*1*	*2*	*3*	*4*
1	2	1	0	0
2	3	1	0	0
3	4	0	0	0
4	1	1	0	0

Run length **90°**

90°	*1*	*2*	*3*	*4*
1	4	0	0	0
2	3	0	0	0
3	4	1	0	0
4	3	0	0	0

Figure 9. An example showing a 4×4 image having four gray levels (1-4) and the resulting gray level run length matrices for two directions.

Different numerical measurements of texture can be estimated from this matrix. The advantage of this analysis is that it provides textural information while incorporating structural information while the calculation is done. As a result of this an explanation of the GLCM features' behavior is found here. For example, an image that has a high number of long runs results in a low entropy value and a high homogeneity value, while the opposite is also true. In [26], the authors suggested that the gray-level values to be grouped into 8 sets (levels) for a 64-levels image, and the run lengths into 6 sets for a 64 by 64 image. We believe the reason behind this is to avoid irrelevant counting of very small runs and very close values of intensity levels, which may contribute in a negative way to the analysis. Since our analysis is applied over the largest connected volume with no background intensity variation or noise, we need every single run length of the volume to be counted. Also, due to having 256 intensity levels, we grouped the gray-level values into 16 different sets. The following five features are described for further explanation.

i) *Short Run Emphasis (SRE)*

This feature measures and emphasizes the short runs in the image, and it is calculated by

$$SRE = \frac{\sum_{i=i}^{N}\sum_{j=1}^{M}\frac{R(i,j)}{j^2}}{\sum_{i=1}^{N}\sum_{j=1}^{M}R(i,j)} \tag{6}$$

where N and M are the row number and the column number of the GLRLM respectively, while R(i,j) is the entry value at location (i,j). A higher value corresponds to a higher amount of short runs in the image, which indicates that the image contains a heterogeneous and irregular texture due to a busy structure.

ii) *Long Run Emphasis (LRE)*

This feature emphasizes the long runs in the image, and it is calculated by

$$LRE = \frac{\sum_{i=i}^{N}\sum_{j=1}^{M} j^2 R(i,\, j)}{\sum_{i=1}^{N}\sum_{j=1}^{M} R(i,\, j)} \tag{8}$$

where higher values correspond to a higher amount of long runs in the image, which indicates that the image contains bigger regions of similar structural texture.

iii) *Gray Level Non-uniformity (GLN)*

The output of this function measures the intensity variation throughout an image, and it is calculated by

$$GLN = \frac{\sum_{i=i}^{N}\left(\sum_{j=1}^{M} R(i,\, j)\right)^2}{\sum_{i=1}^{N}\sum_{j=1}^{M} R(i,\, j)} \tag{9}$$

The lowest value occurs when the runs of the intensity levels are equally distributed throughout the image, higher values correspond to a fine textural structure.

iv) *Run Length Non-uniformity (RLN)*

This feature measures the distribution of the runs throughout the lengths in the image, and it is defined by

$$RLN = \frac{\sum_{j=i}^{M}\left(\sum_{i=1}^{N} R(i,\, j)\right)^2}{\sum_{i=1}^{N}\sum_{j=1}^{M} R(i,\, j)} \tag{10}$$

The function has a low value when the image has a single intensity value, since the distribution of the runs is equal throughout the length.

v) *Run Percentage (RP)*

The output of this function is a ratio of the total number of the runs to the total number of pixels K in the image and it is calculated by

$$RP = \frac{\sum_{i=i}^{N} \sum_{j=1}^{M} R(i, j)}{K} \tag{11}$$

where K is also known as the total possible runs if all the intensities have a run length of one. By combining the two previously mentioned methods, nine different parameters evaluated in nine directions provide us with a complete picture of how the characteristics of samples exposed to different regimes differ from each other. For better understanding of textural parameters, we included synthetic images that explain the differences between the textural parameters in Appendix B.

3.4 Volumetric Quantification

Volumetric parameters were evaluated on the three-dimensional binary version of the images to quantify the morphological information of the induced vasculature networks. Features such as growth direction and volume percentage are presented in this section. We also utilized the two-dimensional z-projection images to estimate the tortuosity and to provide length and angle measurements as additional, but important features.

3.4.1. Growth Direction

This parameter is computed in order to find in which direction the branching network is growing. To evaluate this parameter, an average run length algorithm was also utilized in the nine directions described in Table 1. Higher values result when longer connected regions are examined. For example, if we measure the growth in XY-plane with 0^o between two different objects, the object with the higher value will have a larger connected object in that direction.

3.4.2 Volume Percentage (VP)

This feature measures how much the extracted volume covers from the total size of the sample, and it is calculated by dividing the number of voxels of the extracted volume of interest over the total number of voxels of the sample. This analysis gives us an indication of how changes in frequency and pressure regimes will affect the size of the formed network structures. The actual size of each volume can be found by multiplying the volume of voxels by the spatial dimension of each voxel mentioned in Section 2.1.

3.4.3 Tortuosity

This feature is generally used in estimating the retinal blood vessels curvature, which provides an indication about retinal diseases since normal vessels tend to be straight and gently curved [27]. Different methods were reported in the literature to estimate this feature [27,28,29]. The method named Arc-Chord Ratio (ACR) is used in this work, which is calculated as follows: assume a line segment *S*, as shown in Figure 10, has an Arc length *L* and a chord length *C*, then the tortuosity τ (S) is computed as

$$\tau(S) = \frac{L}{C} \tag{12}$$

where *L* is computed as the sum of the Euclidean distances between the connected pixels of the line segment, while *C* is calculated as the Euclidean distance between the end points of the same segment. This ratio equals 1 for straight line and ∞ for a circle.

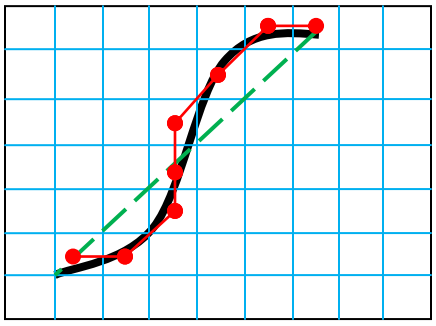

Figure 10. A graph shows a line segment *S* (black) with the digital Euclidean Arc length (red) and the digital Euclidean chord length (green).

In our work, in order to estimate the tortuosity, many steps are taken to find both distances to calculate this feature. The user has to select the region for which he/she wants to estimate this feature manually, and then a thinning algorithm that simplifies the structure into lines is applied. The lines are then separated into different segments (branches) in order to find the end-points. By labeling the different line segments and

extracting the end points, the distance estimation then becomes an easy step and the tortuosity is calculated. The following Figure shows the tortuosity estimation process.

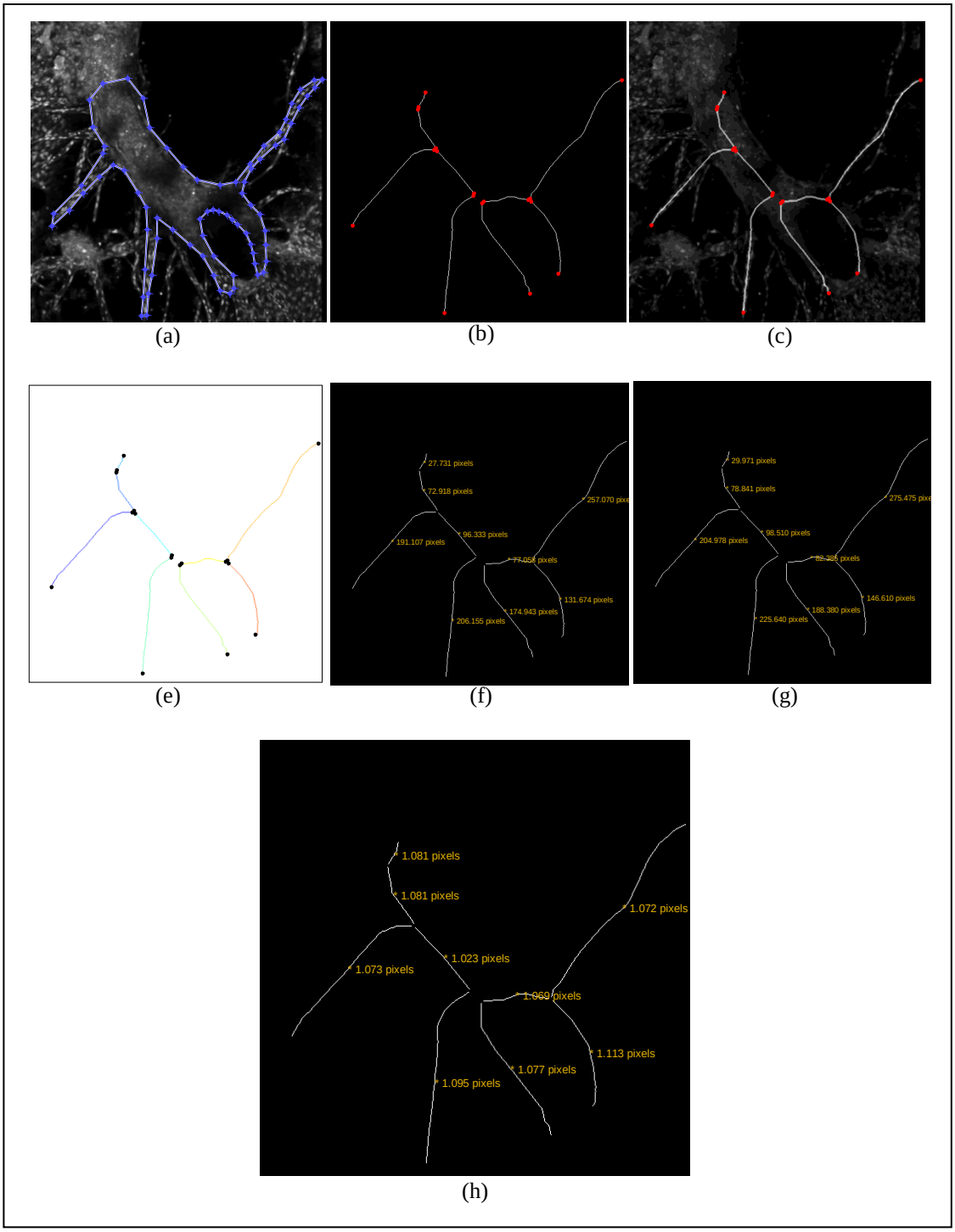

Figure 11. Image (a) shows the user's selection, (b) shows the extracted line segments and the end-points after the thinning step, (c) lines segments are overlaid on the original structure for user's revision, (e) the labeled line segments, (f) the estimation of the Arc length, (g) the estimation of the chord length, and (h) the final tortuosity results.

3.4.3 Length and Angle Estimation

These measurements are also estimated by utilizing the z-projection images. The user will draw a line over the structure that he/she wants to find the value for, then the algorithm will find the distance between the end-points of the line as the length in pixels, while the angle is estimated by finding the angle between the drawn line and the positive x-axis. Figure 12 shows an example of the user selection and the estimated measurements.

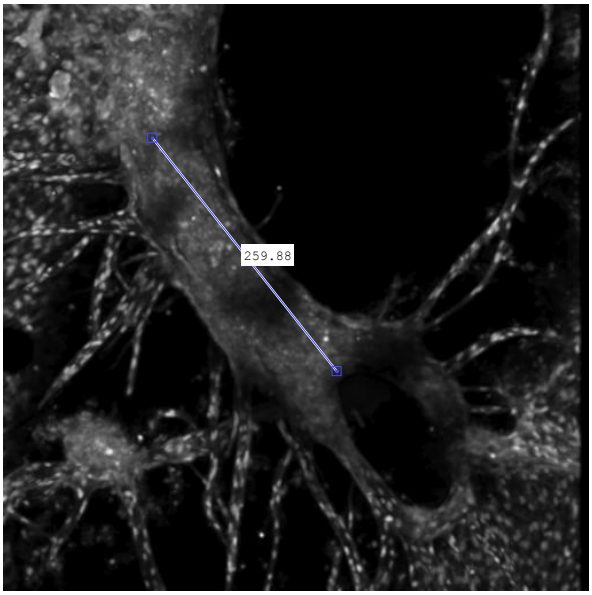

(a)

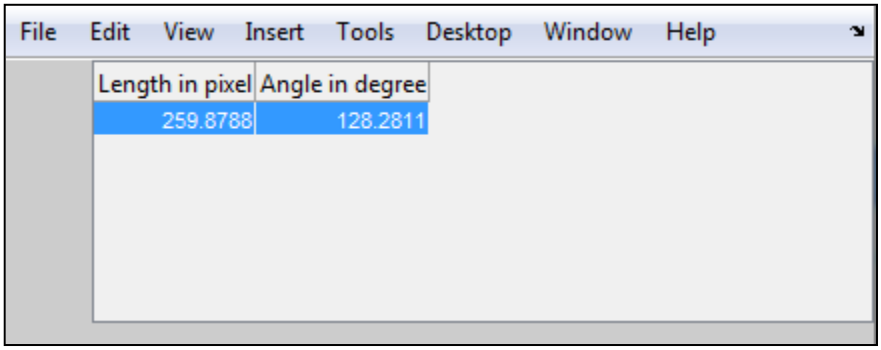

(b)

Figure 12. Image (a) shows the user's input as a blue line, and (b) shows the output table contains the length and the angle results.

3.5 Volume Visualization

In order for scientists working in microscopy to get the full benefits of our tool, a three-dimensional visualization is needed. Using the MATLAB function to produce a volume of approximately 400 images, it took the algorithm close to 1 hour to produce an iso-surface rendering, which lacks the appropriate light effect and speed needed to zoom and rotate the volume. In order to boost the three-dimensional reconstruction through MATLAB, a group of researchers developed a three-dimensional reconstruction extension for MATLAB, using the visualization capabilities of VTK called MATVTK [30]. To the best of our knowledge, a step by step manual that helps setting up this tool is not widely available. After collecting information from different places and troubleshooting, we managed to get the tool to work and to be fully integrated with MATLAB. Due to this reason, we are providing a full setup instructions (see Appendix (C) on how to compile VTK and MATVTK from source code and how to integrate it with MATLAB for any further use in any research requires a three-dimensional visualization. Figure 13 shows the isosurface rendering by MATLAB versus the volume rendering by MATLAB using MATVTK.

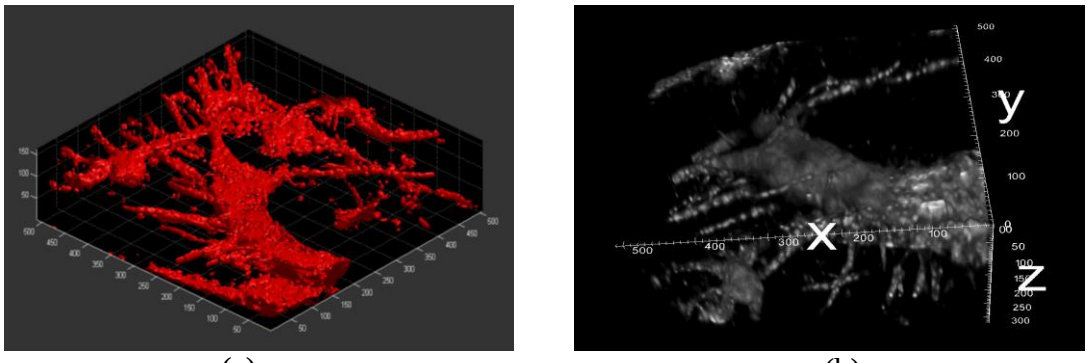

(a) (b)

Figure 13. Image (a) shows the isosurface rendering by MATLAB functions (~ 1h.), (b) shows MATVK volume rendering through MATLAB (~ 10sec.).

Chapter 4 RESULTS

In this paper, we compare different experimental conditions consisting of two different frequency settings and pressure regimes. We use the sham samples as a reference to compare to. Also, since the experiments are independent, the sham results from all experiments were averaged. This step was taken after analyzing each sham sample and not finding noticeable differences among them. Tables 2 and 3 list textural parameters calculated by the (GLCM) and (GLRLM) methods respectively, while Table 4 shows the results calculated for the volumetric analysis.

In Table 2, entropy is highest for the low peak positive pressure cases in both frequency regimes, i.e., 0.1 MPa for 1 MHz, and 0.08 MPa for 2 MHz. These entropy values indicate the disruption of the network appearance compared to the sham values, which show more complex structure. On the other hand, the entropy value for the high peak positive pressure cases in both frequency settings is lowest, since the images contain highly packed sprouts with lower structural complexity. These results are further supported be the fact that energy and homogeneity are lowest, while contrast is maximum in the low-pressure cases, while the opposite is true for the high-pressure cases. By taking a closer look at experiment 2 and 3 (Appendix A), we find that entropy is a bit higher than the averaged sham, while the energy is lower. However, homogeneity and contrast follows the previous observations, while no changes occurred in the low pressure samples. The reason for this is the fact that there is more cell communication in the high pressure samples compared to the sham samples, due to the absence of the pressure effect in the later one. At this stage, we see how the (GLRLM) analysis helps in understanding this issue. By comparing both experiments to the sham results, we find that the high

pressure samples have lower number of short runs, run length non-uniformity, and run percentage, which supports our reasoning above.

In Table 3, the high-pressure samples have lower values of short runs and higher long run values compared to the sham samples. On the other hand, the opposite is true for the low-pressure samples. This indicates that the high-pressure regime tends to form denser, more uniform, and smoother regions with bands and long sprouts. However, the low pressure setting wasn't enough to force the cells to form thick bands, but it was enough to form short branches when comparing to the sham samples. This conclusion is further supported by the difference of the values in the rest of the features. Other parameters presented in the literature [31,32] which will increase the dimensionality and the complexity in interpreting the results were not included.

Table 4 shows that the high-pressure cases have higher volumetric run length values than the low-pressure cases compared to sham samples, except for the z-direction, due to the morphological structure of the low-pressure setting as shown in Figure 14 (a). Also, it is worth mentioning that the ratio between the z-direction run length and the other directions shows that the high-pressure setting tends to form structures in the center of the plate as shown in Figure 14 (b), while the low-pressure samples tends to grow vertically compared to sham networks which lay down at the bottom of the plate as shown in Figure 14 (c).

The absence of (USWF) on the sham samples result in a lower rate of biological communication between the cells, which is supported by the fact that they have lower volume percentage (VP) in Table 4. On the other hand, low-pressure samples have the highest values of (VP), since the pressure is enough for the cells to communicate, but not

enough to pack them into thick bands. The values for the high-pressure samples tend to be in-between except for the 2MHz samples, which we noticed that they were always lower in this case. We relate this observation to the effect of changing the frequency to a higher setting, which induces the formation of bands more than in the 1MHz samples.

The overall results show that the high-pressure samples have smoother, more uniform, longer, and densely packed structure, while the low-pressure samples tends to have non-uniform, more heterogeneous, shorter, and unpacked network structure. Therefore, the quantitative results presented in this work obtained using textural and volumetric analysis of three-dimensional vascular structures in engineered tissues support the qualitative observations made in [18], that different vascular network morphologies are formed when low versus high pressure amplitudes were used to organize cells within the tissue constructs. Figure 15 shows the GUI that was developed and used to produce these results.

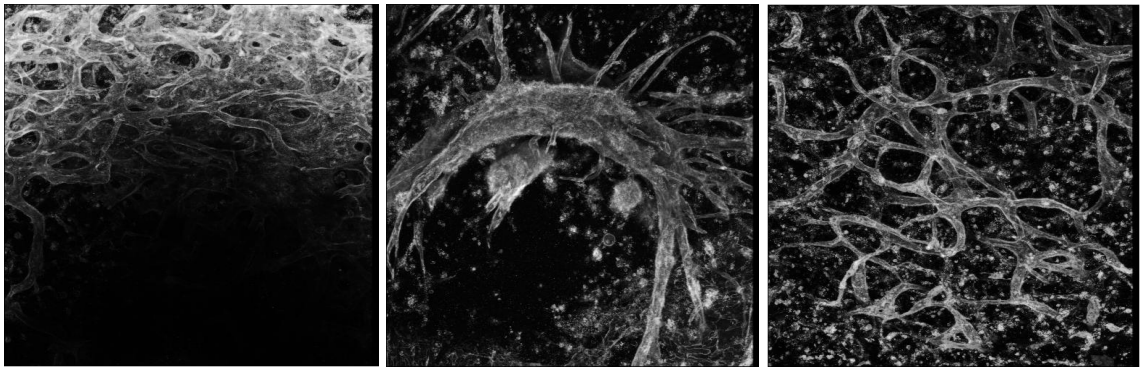

(a) (b) (c)

Figure. 14. The figure shows different projections of cell formation due to the pressure exposure. (a) shows low-pressure exposure with shorter branches. (b) shows high-pressure exposure which forms thick bands in the center of the gel, while (c) shows the sham formation with less structure at the bottom of the gel.

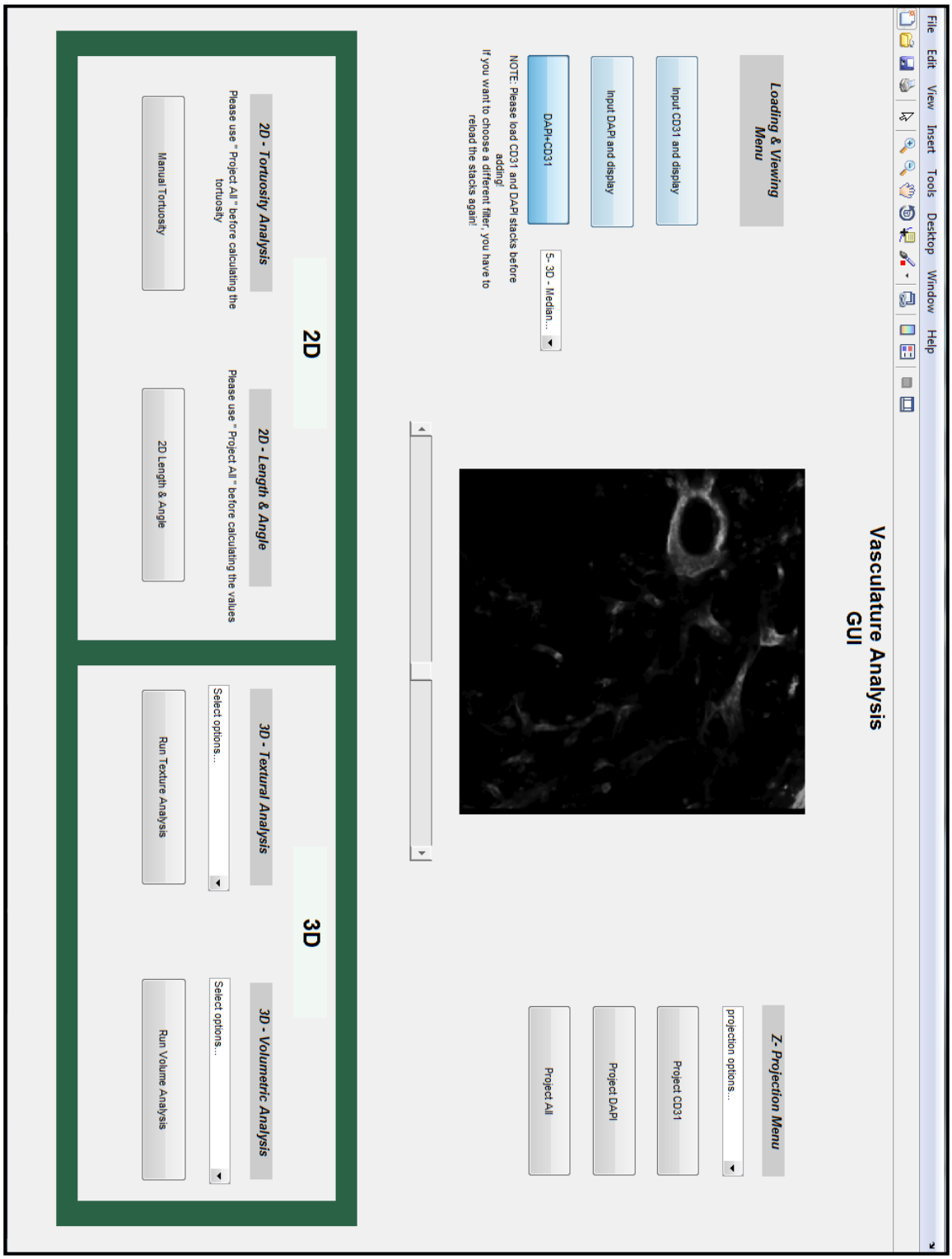

Figure. 15. The figure shows the developed GUI used to produce the results. The GUI includes all the needed operations to analyze the vascular network using the proposed work.

Table 2. Results obtained during the GLCM textural analysis, where tables 2.1 - 2.5 are the results for different frequency and pressure settings. Please see section 3.3 for abbreviations

Table 2.1. GLCM results for 1MHz - 0.3 MPa

Exp.1 - High pressure - 1MHz				
Orientation	**ENT.**	**ENE.**	**HOM.**	**CON.**
(XY)- 0	1.9512	0.7198	0.9149	3.5965
(XY)- 90	1.929	0.7206	0.9182	3.1682
(XY)- 45	2.0206	0.7167	0.9034	6.0546
(XY)- 135	2.025	0.7161	0.9034	6.462
(YZ)- 90	1.77	0.7255	0.9396	0.7159
(YZ)- 45	1.9716	0.7189	0.9104	3.9726
(YZ)-135	1.9787	0.7188	0.9086	4.2206
(XZ)- 45	1.9595	0.7195	0.9113	3.6821
(XZ)- 135	1.9534	0.7197	0.9128	3.6626
MEAN	**1.951**	**0.71951**	**0.91362**	**3.94834**

Table 2.2. GLCM results for 1MHz - 0.1 MPa

Exp.1 - Low pressure - 1MHz				
Orientation	**ENT.**	**ENE.**	**HOM.**	**CON.**
(XY)- 0	2.9018	0.6172	0.8485	15.4461
(XY)- 90	2.9571	0.6147	0.8412	21.1111
(XY)- 45	3.07	0.6081	0.8259	36.8129
(XY)- 135	3.0313	0.6108	0.8307	31.734
(YZ)- 90	2.5638	0.627	0.8934	2.3344
(YZ)- 45	2.9122	0.6163	0.8464	15.6294
(YZ)-135	2.9395	0.6156	0.841	18.72
(XZ)- 45	2.9663	0.614	0.8392	21.4786
(XZ)- 135	2.9872	0.6131	0.8355	24.1574
MEAN	**2.92547**	**0.6152**	**0.84464**	**20.8249**

Table 2.3. GLCM results Averaged SHAM

SHAM-Avearge				
Orientation	**ENT.**	**ENE.**	**HOM.**	**CON.**
(XY)- 0	2.44242	0.66688	0.87004	12.021
(XY)- 90	2.46008	0.66612	0.8666	13.1585
(XY)- 45	2.56048	0.65868	0.85284	23.5968
(XY)- 135	2.56248	0.65862	0.8525	23.9476
(YZ)- 90	2.0993	0.68074	0.91596	1.29312
(YZ)- 45	2.45952	0.66612	0.86584	13.2331
(YZ)-135	2.4538	0.66638	0.8669	12.76
(XZ)- 45	2.47292	0.66552	0.86348	14.4308
(XZ)- 135	2.47114	0.6655	0.86364	13.8104
MEAN	**2.44246**	**0.66606**	**0.86864**	**14.2501**

Table 2.4. GLCM results for 2MHz - 0.2 MPa

Exp.4 - High pressure - 2MHz				
Orientation	**ENT.**	**ENE.**	**HOM.**	**CON.**
(XY)- 0	2.1223	0.7145	0.9023	6.1417
(XY)- 90	2.1443	0.7139	0.8981	7.2151
(XY)- 45	2.2112	0.7105	0.8887	11.7976
(XY)- 135	2.2267	0.7099	0.8869	13.4293
(YZ)- 90	1.9822	0.7188	0.9171	1.6072
(YZ)- 45	2.1605	0.713	0.8948	7.506
(YZ)-135	2.166	0.7127	0.8939	7.5108
(XZ)- 45	2.1857	0.7121	0.8906	8.9442
(XZ)- 135	2.1712	0.7127	0.8927	8.1964
MEAN	**2.15223**	**0.71312**	**0.89612**	**8.0387**

Table 2.5. GLCM results for 2MHz - 0.08 MPa

Exp.4 - Low pressure - 2MHz				
Orientation	**ENT.**	**ENE.**	**HOM.**	**CON.**
(XY)- 0	3.3451	0.5844	0.8166	23.9631
(XY)- 90	3.3603	0.584	0.8137	25.7734
(XY)- 45	3.4631	0.5778	0.8021	40.6454
(XY)- 135	3.5091	0.5758	0.7963	51.0351
(YZ)- 90	2.9009	0.5969	0.8732	2.8079
(YZ)- 45	3.3695	0.5833	0.8124	26.4812
(YZ)-135	3.3632	0.5831	0.8133	24.8068
(XZ)- 45	3.374	0.5833	0.8117	27.1389
(XZ)- 135	3.3856	0.5824	0.8092	27.7396
MEAN	**3.3412**	**0.583444**	**0.8165**	**27.8213**

Table 3. Results obtained during the GLRLM textural analysis, where tables 3.1 – 3.5 are the results for different frequency and pressure settings. Please see section 3.3 for abbreviations

Table 3.1. GLRLM results for 1MHz - 0.3 MPa

Exp.1 - High pressure - 1MHz					
Orientation	SRE.	LRE.	GLN.	RLN.	RP
(XY) - 0	0.1838	1.27E+04	1.36E+03	439.0002	0.0268
(XY) - 90	0.1583	1.31E+04	1.20E+03	343.4721	0.0239
(XY) - 45	0.2293	5.83E+03	1.83E+03	707.2975	0.0354
(XY) - 135	0.2353	5.87E+03	1.89E+03	733.4422	0.0361
(YZ) - 90	0.0556	1.65E+04	583.7711	137.812	0.0181
(YZ) - 45	0.1638	5.83E+03	1.10E+03	354.0597	0.0331
(YZ) - 135	0.163	7.05E+03	1.06E+03	339.4128	0.0319
(XZ) - 45	0.1966	4.60E+03	1.12E+03	385.4803	0.0342
(XZ) - 135	0.2064	4.13E+03	1.14E+03	416.6471	0.0356
Mean	**0.1769**	**8.40E+03**	**1.25E+03**	**428.5138**	**0.03057**

Table 3.2. GLRLM results for 1MHz - 0.1 MPa

Exp.1 - Low pressure - 1MHz					
Orientation	SRE.	LRE.	GLN.	RLN.	RP
(XY) - 0	0.3551	3.60E+03	2.30E+03	2.17E+03	0.0602
(XY) - 90	0.3814	3.43E+03	2.55E+03	2.58E+03	0.0659
(XY) - 45	0.4326	1.69E+03	3.32E+03	4.01E+03	0.0839
(XY) - 135	0.4265	1.76E+03	3.08E+03	3.74E+03	0.0798
(YZ) - 90	0.0812	1.55E+04	855.3274	365.8829	0.0329
(YZ) - 45	0.3115	5.20E+03	1.99E+03	1.85E+03	0.0739
(YZ) - 135	0.3256	4.73E+03	2.10E+03	2.21E+03	0.079
(XZ) - 45	0.3421	1.86E+03	1.67E+03	1.47E+03	0.0667
(XZ) - 135	0.3724	1.72E+03	1.81E+03	1.92E+03	0.0748
Mean	**0.33649**	**4.39E+03**	**2.18E+03**	**2.26E+03**	**0.06857**

Table 3.3. GLRLM results for Averaged SHAM

SHAM - Average					
Orientation	SRE.	LRE.	GLN.	RLN.	RP
(XY) - 0	0.32782	9.20E+03	2458.08	1797.5	0.05346
(XY) - 90	0.34236	8696.18	2605.1	1956.24	0.05616
(XY) - 45	0.37988	4283.64	3460.58	2972.1	0.07148
(XY) - 135	0.38158	4225.72	3479.36	3009.02	0.072
(YZ) - 90	0.09742	9988.48	745.41524	240.5786	0.02576
(YZ) - 45	0.34278	2443.06	2031.32	1594.3	0.06456
(YZ) - 135	0.33806	2440.32	2036.38	1532.88	0.06388
(XZ) - 45	0.3264	1944.6	1954.74	1479.347	0.06242
(XZ) - 135	0.3202	2019.98	1923.54	1409.669	0.06122
Mean	**0.31739**	**5.03E+03**	**2.30E+03**	**1.78E+03**	**0.05899**

Table 3.4. GLRLM results for 2MHz - 0.2 MPa

Exp.4 - Highe pressure - 2MHz					
Orientation	SRE.	LRE.	GLN.	RLN.	RP
(XY) - 0	0.2533	1.08E+04	1.29E+03	784.924	0.033
(XY) - 90	0.2696	8.41E+03	1.38E+03	952.1899	0.036
(XY) - 45	0.3148	4.39E+03	1.84E+03	1.43E+03	0.0459
(XY) - 135	0.3277	4.31E+03	1.92E+03	1.57E+03	0.0479
(YZ) - 90	0.1008	1.02E+04	723.5229	385.2596	0.0278
(YZ) - 45	0.3053	3.53E+03	1.35E+03	1.13E+03	0.0503
(YZ) - 135	0.2749	4.09E+03	1.25E+03	910.5132	0.0464
(XZ) - 45	0.2841	4.60E+03	1.24E+03	888.1834	0.0455
(XZ) - 135	0.293	3.98E+03	1.28E+03	918.7763	0.0463
Mean	**0.26928**	**6.03E+03**	**1.37E+03**	**997.194**	**0.04212**

Table 3.5. GLRLM results for 2MHz - 0.08 MPa

Exp.4 - Low pressure - 2MHz					
Orientation	SRE.	LRE.	GLN.	RLN.	RP
(XY) - 0	0.3453	3.12E+03	2.69E+03	2.39E+03	0.0687
(XY) - 90	0.3505	3.28E+03	2.79E+03	2.51E+03	0.0702
(XY) - 45	0.386	1.73E+03	3.46E+03	3.47E+03	0.0849
(XY) - 135	0.4281	1.35E+03	3.80E+03	4.53E+03	0.0946
(YZ) - 90	0.0631	1.07E+04	873.3615	311.065	0.0314
(YZ) - 45	0.3198	3.31E+03	2.23E+03	2.03E+03	0.0786
(YZ) - 135	0.3299	2.88E+03	2.31E+03	2.11E+03	0.0811
(XZ) - 45	0.3549	1.23E+03	2.09E+03	2.03E+03	0.0795
(XZ) - 135	0.3441	1.18E+03	2.08E+03	1.87E+03	0.0772
Mean	**0.32463**	**3.20E+03**	**2.48E+03**	**2.36E+03**	**0.07402**

Table 4. Results obtained during the volumetric analysis, where tables 4.1 - 4.5 are the results for different frequency and pressure settings.

Table 4.1. Volumetric results for 1MHz - 0.3 MPa

Exp.1 - High pressure - 1MHz	
Orientation	*Pixles*
(XY) - 0	21.1368
(XY) - 90	22.4485
(XY) - 45	15.7031
(XY) - 135	15.0604
(YZ) - 90	41.7824
(YZ) - 45	18.2372
(YZ) - 135	18.0696
(XZ) - 45	18.9129
(XZ) - 135	19.1233
% Volume	18.25

Table 4.2. Volumetric results for 1MHz - 0.1 MPa

Exp.1 - Low pressure - 1MHz	
Orientation	*Pixles*
(XY) - 0	18.9277
(XY) - 90	16.8172
(XY) - 45	11.9076
(XY) - 135	13.2618
(YZ) - 90	51.3062
(YZ) - 45	17.473
(YZ) - 135	16.8228
(XZ) - 45	15.8074
(XZ) - 135	15.1676
% Volume	19.94

Table 4.3. Volumetric results for Averaged SHAM

SHAM-Avg	
Orientation	*Pixles*
(XY) - 0	12.72636
(XY) - 90	11.9908
(XY) - 45	8.70414
(XY) - 135	8.7624
(YZ) - 90	39.7808
(YZ) - 45	11.71306
(YZ) - 135	11.91068
(XZ) - 45	11.18594
(XZ) - 135	11.20414
% Volume	16.106

Table 4.4. Volumetric results for 2MHz - 0.2 MPa

Exp.4 - High pressure - 2MHz	
Orientation	*Pixles*
(XY) - 0	26.638
(XY) - 90	25.5153
(XY) - 45	18.8382
(XY) - 135	17.9689
(YZ) - 90	46.8313
(YZ) - 45	22.344
(YZ) - 135	21.7345
(XZ) - 45	21.0303
(XZ) - 135	22.0405
% Volume	14.97

Table 4.5. Volumetric results for 2MHz - 0.08 MPa

Exp.4 - Low pressure - 2MHz	
Orientation	*Pixles*
(XY) - 0	18.4519
(XY) - 90	16.9146
(XY) - 45	12.9795
(XY) - 135	12.1075
(YZ) - 90	56.3101
(YZ) - 45	17.0968
(YZ) - 135	17.0008
(XZ) - 45	16.1014
(XZ) - 135	15.4534
% Volume	22.35

Chapter 5 CONCLUSIONS AND FUTURE WORK

In this work, a tool that analyzes three-dimensional vasculature networks in engineered tissues alongside providing a three-dimensional volume rendering was proposed. The algorithm used textural and volumetric parameters for quantitative analysis to provide a more objective and reliable monitoring as well as a quantitative comparison between the structures. We showed that combining two different textural quantification methods provide a comprehensive overview about the structure's heterogeneity. We also showed that expanding the analysis to cover nine orientations in quantifying textural and volumetric features, enabled us to capture full three-dimensional changes happen throughout our samples. Other volumetric parameters such as porosity, permeability, and diffusion distance were not included, since they don't serve the purpose of comparing totally different structures. Parameters such as tortuosity, length, and angle that provides more information about the induced structures using the z-projection version of the stacks were included. The algorithm provided a fast three-dimensional volume rendering by linking MATLAB and VTK using the newly developed tool named MATVTK. The algorithm is provided with a standalone (GUI) written in MATLAB, which will allow the scientists to interact with the algorithm without the need of understanding the code. The (GUI) also provides other functions such as viewing, filtering, or projecting the samples using different techniques. Future work includes investigating different sophisticated segmentation techniques beside the effect of other three-dimensional volumetric parameters such as Three-dimensional Fractal Dimension (3D-FD), which is commonly used in medical imaging [33], and Three-dimensional structural similarity features in order to provide more structural information are considered.

Bibliography

[1] P.R. Barber, B. Vojnovic, J. Kelly, C.R. Mayes, P. Mayes, M. Woodcock, and M.C. Joiner, "Automated Counting of Mammalian Cell Colonies," Physics in Medicine and Biology, vol., 64, pp.63-76, (2001).

[2] N. Harder, M. Bodnar, R. Elis, D.L. Spector, and K. Rohr, "3D Segmentation and Quantification of Mouse Embryonic Stem Cells in Fluorescence Microscopy Images ," Biomedical Imaging: From Nano to Macro, 2011 IEEE International Symposium on, pp.216-219, (2011).

[3] J. Diamond, N.H. Anderson, P.H. Bartels, R. Montironi, and P.W. Hamilton, "The Use of Morphological Characteristics and Texture Analysis in the Identification of Tissue Composition in Prostatic Neoplasia," Hum. Pathol, vol., 35, pp.1121-1131, (2004).

[4] R.M. Haralick, K. Shanmuga, and I. Dinstein, "Textural Features for Image Classification," IEEE Transactions on Systems, Man and Cybernetics SMC3, pp.610-621, (1973).

[5] F. Cassot, F. Lauwers, C. Fouard, S. Prohaska, and V. Lauwers-Cances, "A Novel Three-dimensional Computer-assisted Method for A Quantitative Study of Microvascular Networks of the Human Cerebral Cortex," Microcirculation, vol., 13, pp.1–18, (2006).

[6] P.R. Barber, S.M. Ameer-Beg, B. Vojnovic, R.J. Hodgkiss, G.M. Tozer, J. Wilson, and V.E. Prise, "3D Imaging and Quantification of Complex Vascular Networks," Proceedings of SPIE-OSA Biomedical Optics, SPIE, vol., 5139, (2003).

[7] X.M. Yang, H. Beyenal, G. Harkin,, and Z. Lewandowski, "Quantifying Biofilm Structure Using Image Analysis," Journal of Microbiological Methods, Elsevier, pp.109-119, (2000).

[8] A. Heydron, A.T. Nielsen, M. Hentzer, C. Sternberg, M. Givskov, B.K. Ersboll, and S. Molin, "Quantification of Biofilm Structure by the Novel Computer Program COMSTAT," Journal of Microbiology, pp.2395-2407, (2000).

[9] H. Beyenal, C. Donovan, Z. Lewandowski, and G. Harkin, "Three-dimensional Biofilm Structure Quantification," Journal of Microbiological Methods, Elsevier, pp.395-413, (2004).

[10] H.J. Choi, I.H. Choi, T.Y. Kim, and H.K. Choi, "A Computerized Program for Three-dimensional Visualization and Quantitative Analysis of Cell Nuclei," Enterprise Networking and Computing in Healthcare Industry, Proceedings. 6th International Workshop, pp.83- 87, (2004).

[11] F. Scarpa, D. Fiorin, and A. Ruggeri, "In Vivo Three-dimensional Recon-Struction of the Cornea From Confocal Microscopy Images," Conference Proceedings of IEEE Engineering in Medicine and Biology Society, pp.747–750, (2007).

[12] J. Wu, B. Rajwa, D.L. Filmer, C.M. Hoffmann, B. Yuan, C. Chiang, et al., "Automated Quantification and Reconstruction of Collagen Matrix From 3D Confocal Datasets," Journal of Microscopy, vol., 210, pp.158-165, (2003).

[13] E. Kaczmarek, and R. Strzelczyk, "From Two to Three-dimensional Visualization of Structures in Light and Confocal Microscopy – Applications for Biomedical Studies," Multidisciplinary Microscopy Research and Education, pp.289-295, (2005).

[14] H.J. Choi, T.Y. Kim, N.H. Cho, G.B. Jeong, Y. Huh, and H.K. Choi, "Three-dimensional Quantitative Analysis of Cell Nuclei for Grading Renal Cell Carcinoma," Enterprise networking and Computing in Healthcare Industry, HEALTHCOM. Proceedings of 7th International Workshop, pp.179- 186, (2005).

[15] H. C. Peng, Z. C. Ruan, F. H. Long, J. H. Simpson, and E. W. Myers, "V3D Enables Real-Time 3D Visualization and Quantitative Analysis of Large-Scale Biological Image Data Sets," Nature Biotechnology, vol., 28, pp.348, (2010).

[16] K.A. Garvin, D.C. Hocking, and D. Dalecki, "Controlling the Spatial Organization of Cells and Extracellular Matrix Proteins in Engineered Tissues Using Ultrasound Standing Wave Fields," Ultrasound in Medicine & Biology, Elsevier, pp.1919-1932, (2010).

[17] K.A. Garvin, D. Dalecki, and D.C. Hocking, "Vascularization of Three-Dimensional Collagen Hydrogels Using Ultrasound Standing Wave Fields," Ultrasound in Medicine & Biology, Elsevier, vol., 37, pp.1835-1864, (2011).

[18] K.A. Garvin, D. Dalecki, and D.C. Hocking, "Vascular Network Formation Within Collagen Hydrogels Fabricated With Different Spatial Organizations of Endothelial Cells Using Ultrasound-Based Cell Patterning Techniques," The North American Vascular Biology Organization (NAVBO), Hyannis, MA, (2011).

[19] Sonka, Hlavac, and Boyle, Digital Image Processing and Computer Vision, Cengage Learning, pp.571-580, (2008).

[20] R. C. Gonzalez and R. E. Woods, Digital Image Processing, Prentice Hall, Upper Saddle River, N. J., 2002; Tekhnosfera, Moscow, (2005).

[21] S. M. Pizer, E. P. Amburn, J. D. Austin, R. Cromartie, A. Geselowitz, T. Greer, B. H. Romeny, J. B. Zimmerman, and K. Zuiderveld, "Adaptive Histogram Equalization and Its Variations," Computer Vision, Graphics, and Image Processing, pp.355–368, (1987).

[22] S. Rajagopalan, M.J. Yaszemski, and R. Robb, "Evaluation of Thresholding Techniques for Segmenting Scaffold Images in Tissue Engineering," SPIE Proceedings on Medical Imaging, pp.1456–1465, (2004).

[23] M. Tuceryan and A.K. Jain, "Texture Analysis," Handbook Pattern Recognition and Computer Vision (2nd Edition), C.H. Chen, L.F. Pau, and P.S.P. Wang, eds., ch. 2, pp. 235–276. Singapore: World Scientific, (1998).

[24] R.M. Haralick, K. Shanmuga, I. Dinstein, "Textural Features for Image Classification," IEEE Transactions on Systems, Man and Cybernetics SMC3, pp.610-621, (1973).

[25] S. Theodoridis, K. Koutroumbas, "Pattern Recognition," 4th Edition, Academic Press, (2008).

[26] M.M. Galloway, "Texture Analysis Using Gray Level Run Lengths," Computer Graphics and Image processing, Elsevier, vol., 4, 172-179, (1975).

[27] W. Hart, M. Goldbaum, B. Cote, P. Kube, and M. Nelson, "Automated Measurement of Retinal Vascular Tortuosity," AMIA Annual Symposium, (1997).

[28] W. Hart, M. Goldbaum, B. Cote, P. Kube, and M. Nelson "Measurement and Classification of Retinal Vascular Tortuosity," International Journal of Medical Informatics, vol., 53, pp. 239–252, (1999).

[29] C. Sinthanayothin, P. Panitsuk, and B. Uyyanonvara, "Automatic retinal vessel tortuosity measurement," Electrical Engineering/Electronics, Computer, Telecommunications and Information Technology (ECTI-CON), International Conference, pp.505-507, (2010).

[30] E. Birngruber, R. Donner, and G. Langs, "MATVTK - 3D Visualization for MATLAB," Proceedings of the MICCAI 2009 Workshop on systems and architectures for CAI, (2009).

[31] X. Tang, "Texture information in run-length matrices," IEEE Transactions on Image Processing, pp.1602-1609 (1998).

[32] F. Albregtsen, B. Nielsen, and H.E. Danielsen, "Adaptive Gray Level Run Length Features from Class Distance Matrices," International Conference on Pattern Recognition, vol., 3, pp.3746-3749, (2000).

[33] L. Zhang, J.Z. Liu, D. Dean, V. Sahgal, and G.H. Yue, " A Three-dimensional Fractal Analysis Method for Quantifying White Matter Structure in Human Brain," Journal of Neuroscience Methods, vol., 150, pp.242-253, (2006).

Appendix A

Table 5. Results obtained during the GLCM textural analysis, where tables 5.1 - 5.6 are the results for experiment 1,2, and 3, while tables 5.7 - 5.10 are for experiment 4 and 5. Table 5.11 is for averaged sham.

Table 5.1. GLCM results for Exp.1. 1MHz - 0.3MPa

Exp.1 - High pressure - 1MHz				
Orientation	**ENT.**	**ENE.**	**HOM.**	**CON.**
(XY)- 0	1.9512	0.7198	0.9149	3.5965
(XY)- 90	1.929	0.7206	0.9182	3.1682
(XY)- 45	2.0206	0.7167	0.9034	6.0546
(XY)- 135	2.025	0.7161	0.9034	6.462
(YZ)- 90	1.77	0.7255	0.9396	0.7159
(YZ)- 45	1.9716	0.7189	0.9104	3.9726
(YZ)-135	1.9787	0.7188	0.9086	4.2206
(XZ)- 45	1.9595	0.7195	0.9113	3.6821
(XZ)- 135	1.9534	0.7197	0.9128	3.6626
MEAN	**1.951**	**0.71951**	**0.91362**	**3.94834**

Table 5.2. GLCM results for Exp.1. 1MHz - 0.1MPa

Exp.1 - Low pressure - 1MHz				
Orientation	**ENT.**	**ENE.**	**HOM.**	**CON.**
(XY)- 0	2.9018	0.6172	0.8485	15.4461
(XY)- 90	2.9571	0.6147	0.8412	21.1111
(XY)- 45	3.07	0.6081	0.8259	36.8129
(XY)- 135	3.0313	0.6108	0.8307	31.734
(YZ)- 90	2.5638	0.627	0.8934	2.3344
(YZ)- 45	2.9122	0.6163	0.8464	15.6294
(YZ)-135	2.9395	0.6156	0.841	18.72
(XZ)- 45	2.9663	0.614	0.8392	21.4786
(XZ)- 135	2.9872	0.6131	0.8355	24.1574
MEAN	**2.92547**	**0.6152**	**0.84464**	**20.8249**

Table 5.3. GLCM results for Exp.2. 1MHz - 0.3MPa

Exp.2 - High pressure - 1MHz				
Orientation	**ENT.**	**ENE.**	**HOM.**	**CON.**
(XY)- 0	2.5471	0.6148	0.8888	4.4402
(XY)- 90	2.5819	0.6135	0.8854	5.6704
(XY)- 45	2.6791	0.6084	0.8688	9.4309
(XY)- 135	2.6887	0.608	0.8661	9.2065
(YZ)- 90	2.2579	0.623	0.9326	0.7369
(YZ)- 45	2.5556	0.6139	0.8865	4.4902
(YZ)-135	2.5893	0.613	0.8794	5.2693
(XZ)- 45	2.6046	0.6123	0.8798	6.0846
(XZ)- 135	2.6071	0.6121	0.8796	6.1247
MEAN	**2.56792**	**0.61322**	**0.88522**	**5.71708**

Table 5.4. GLCM results for Exp.2. 1MHz - 0.1MPa

Exp.2 - Low pressure - 1MHz				
Orientation	**ENT.**	**ENE.**	**HOM.**	**CON.**
(XY)- 0	3.6438	0.5275	0.8121	18.4672
(XY)- 90	3.6128	0.5282	0.8173	16.2242
(XY)- 45	3.7788	0.5231	0.7928	32.6237
(XY)- 135	3.7574	0.5238	0.796	30.0095
(YZ)- 90	3.1507	0.5349	0.8899	2.2602
(YZ)- 45	3.6637	0.5262	0.8091	19.2185
(YZ)-135	3.6729	0.5259	0.8068	19.8457
(XZ)- 45	3.6283	0.5271	0.8143	16.755
(XZ)- 135	3.6503	0.5263	0.8113	17.8325
MEAN	**3.61763**	**0.527**	**0.81662**	**19.2485**

Table 5.5. GLCM results for Exp.3. 1MHz - 0.3MPa

Exp.3 - High pressure - 1MHz				
Orientation	**ENT.**	**ENE.**	**HOM.**	**CON.**
(XY)- 0	2.5086	0.6343	0.8858	6.9406
(XY)- 90	2.5169	0.6342	0.8851	7.592
(XY)- 45	2.6169	0.6293	0.8687	13.3562
(XY)- 135	2.6276	0.6292	0.8668	13.6116
(YZ)- 90	2.26	0.6407	0.9238	1.2292
(YZ)- 45	2.5335	0.6329	0.8799	7.5024
(YZ)-135	2.5409	0.6329	0.8792	8.0211
(XZ)- 45	2.5294	0.6332	0.8815	7.6782
(XZ)- 135	2.5585	0.6324	0.8767	9.1318
MEAN	**2.52137**	**0.63323**	**0.88306**	**8.34034**

Table 5.6. GLCM results for Exp.3. 1MHz - 0.1MPa

Exp.3 - Low pressure - 1MHz				
Orientation	**ENT.**	**ENE.**	**HOM.**	**CON.**
(XY)- 0	3.0464	0.6142	0.8456	14.517
(XY)- 90	3.1055	0.6128	0.8366	20.4399
(XY)- 45	3.1935	0.6085	0.8256	31.3562
(XY)- 135	3.2033	0.6084	0.8245	34.144
(YZ)- 90	2.7453	0.6206	0.8824	2.5219
(YZ)- 45	3.0772	0.6126	0.8399	16.0806
(YZ)-135	3.0854	0.6124	0.8385	16.7321
(XZ)- 45	3.1172	0.6117	0.8354	20.6232
(XZ)- 135	3.145	0.6108	0.8296	23.9566
MEAN	**3.07987**	**0.612444**	**0.83979**	**20.0413**

Table 5.7. GLCM results for Exp.4. 2MHz - 0.1MPa

Exp.4 - High pressure - 2MHz				
Orientation	**ENT.**	**ENE.**	**HOM.**	**CON.**
(XY)- 0	2.1223	0.7145	0.9023	6.1417
(XY)- 90	2.1443	0.7139	0.8981	7.2151
(XY)- 45	2.2112	0.7105	0.8887	11.7976
(XY)- 135	2.2267	0.7099	0.8869	13.4293
(YZ)- 90	1.9822	0.7188	0.9171	1.6072
(YZ)- 45	2.1605	0.713	0.8948	7.506
(YZ)-135	2.166	0.7127	0.8939	7.5108
(XZ)- 45	2.1857	0.7121	0.8906	8.9442
(XZ)- 135	2.1712	0.7127	0.8927	8.1964
MEAN	**2.15223**	**0.71312**	**0.89612**	**8.0387**

Table 5.8. GLCM results for Exp.2. 2MHz - 0.08MPa

Exp.4 - Low pressure - 2MHz				
Orientation	**ENT.**	**ENE.**	**HOM.**	**CON.**
(XY)- 0	3.3451	0.5844	0.8166	23.9631
(XY)- 90	3.3603	0.584	0.8137	25.7734
(XY)- 45	3.4631	0.5778	0.8021	40.6454
(XY)- 135	3.5091	0.5758	0.7963	51.0351
(YZ)- 90	2.9009	0.5969	0.8732	2.8079
(YZ)- 45	3.3695	0.5833	0.8124	26.4812
(YZ)-135	3.3632	0.5831	0.8133	24.8068
(XZ)- 45	3.374	0.5833	0.8117	27.1389
(XZ)- 135	3.3856	0.5824	0.8092	27.7396
MEAN	**3.3412**	**0.583444**	**0.8165**	**27.8213**

Table 5.9. GLCM results for Exp.5. 2MHz - 0.1MPa

Exp.5 - High pressure - 2MHz				
Orientation	**ENT.**	**ENE.**	**HOM.**	**CON.**
(XY)- 0	2.276	0.6915	0.8924	7.7318
(XY)- 90	2.2691	0.6918	0.8925	6.7801
(XY)- 45	2.3548	0.6872	0.8802	11.9523
(XY)- 135	2.3823	0.686	0.8766	15.2969
(YZ)- 90	2.0306	0.6993	0.9257	1.1562
(YZ)- 45	2.2991	0.6904	0.8879	8.559
(YZ)-135	2.2973	0.6906	0.8874	8.5996
(XZ)- 45	2.2984	0.6907	0.8869	7.9406
(XZ)- 135	2.2801	0.6912	0.8899	7.3011
MEAN	**2.27641**	**0.69097**	**0.89106**	**8.36862**

Table 5.10. GLCM results for Exp.5. 2MHz - 0.08MPa

Exp.5 - Low pressure - 2MHz				
Orientation	**ENT.**	**ENE.**	**HOM.**	**CON.**
(XY)- 0	3.1227	0.6183	0.8431	17.0884
(XY)- 90	3.1942	0.6163	0.8321	24.9883
(XY)- 45	3.2644	0.6128	0.8242	34.8572
(XY)- 135	3.3074	0.6109	0.8194	43.7068
(YZ)- 90	2.8579	0.6251	0.8732	3.8132
(YZ)- 45	3.168	0.617	0.8342	20.7031
(YZ)-135	3.1532	0.6173	0.8369	19.07
(XZ)- 45	3.2411	0.6147	0.8248	31.5581
(XZ)- 135	3.1897	0.6161	0.8332	23.8034
MEAN	**3.16651**	**0.6165**	**0.83568**	**24.3987**

Table 5.11. GLCM results for Averaged SHAM

SHAM-Avearge				
Orientation	**ENT.**	**ENE.**	**HOM.**	**CON.**
(XY)- 0	2.44242	0.66688	0.87004	12.021
(XY)- 90	2.46008	0.66612	0.8666	13.1585
(XY)- 45	2.56048	0.65868	0.85284	23.5968
(XY)- 135	2.56248	0.65862	0.8525	23.9476
(YZ)- 90	2.0993	0.68074	0.91596	1.29312
(YZ)- 45	2.45952	0.66612	0.86584	13.2331
(YZ)-135	2.4538	0.66638	0.8669	12.76
(XZ)- 45	2.47292	0.66552	0.86348	14.4308
(XZ)- 135	2.47114	0.6655	0.86364	13.8104
MEAN	**2.44246**	**0.66606**	**0.86864**	**14.2501**

Table 6. Results obtained during the GLRLM textural analysis, where tables 6.1 - 6.6 are the results for experiment 1,2, and 3, while tables 6.7 - 6.10 are for experiment 4 and 5. Table 6.11 is for averaged sham.

Table 6.1. GLRLM results for Exp.1. 1MHz - 0.3MPa

Exp.1 - High pressure - 1MHz					
Orientation	SRE.	LRE.	GLN.	RLN.	RP
(XY) - 0	0.1838	1.27E+04	1.36E+03	439.0002	0.0268
(XY) - 90	0.1583	1.31E+04	1.20E+03	343.4721	0.0239
(XY) - 45	0.2293	5.83E+03	1.83E+03	707.2975	0.0354
(XY) - 135	0.2353	5.87E+03	1.89E+03	733.4422	0.0361
(YZ) - 90	0.0556	1.65E+04	583.7711	137.812	0.0181
(YZ) - 45	0.1638	5.83E+03	1.10E+03	354.0597	0.0331
(YZ) - 135	0.163	7.05E+03	1.06E+03	339.4128	0.0319
(XZ) - 45	0.1966	4.60E+03	1.12E+03	385.4803	0.0342
(XZ) - 135	0.2064	4.13E+03	1.14E+03	416.6471	0.0356
Mean	**0.1769**	**8.40E+03**	**1.25E+03**	**428.5138**	**0.03057**

Table 6.2. GLCM results for Exp.1. 1MHz - 0.1MPa

Exp.1 - Low pressure - 1MHz					
Orientation	SRE.	LRE.	GLN.	RLN.	RP
(XY) - 0	0.3551	3.60E+03	2.30E+03	2.17E+03	0.0602
(XY) - 90	0.3814	3.43E+03	2.55E+03	2.58E+03	0.0659
(XY) - 45	0.4326	1.69E+03	3.32E+03	4.01E+03	0.0839
(XY) - 135	0.4265	1.76E+03	3.08E+03	3.74E+03	0.0798
(YZ) - 90	0.0812	1.55E+04	855.3274	365.8829	0.0329
(YZ) - 45	0.3115	5.20E+03	1.99E+03	1.85E+03	0.0739
(YZ) - 135	0.3256	4.73E+03	2.10E+03	2.21E+03	0.079
(XZ) - 45	0.3421	1.86E+03	1.67E+03	1.47E+03	0.0667
(XZ) - 135	0.3724	1.72E+03	1.81E+03	1.92E+03	0.0748
Mean	**0.33649**	**4.39E+03**	**2.18E+03**	**2.26E+03**	**0.06857**

Table 6.3. GLRLM results for Exp.2. 1MHz - 0.3MPa

Exp.2 - High pressure - 1MHz					
Orientation	SRE.	LRE.	GLN.	RLN.	RP
(XY) - 0	0.177	5.40E+03	1.87E+03	553.8733	0.0365
(XY) - 90	0.2198	3.95E+03	2.09E+03	694.5621	0.0396
(XY) - 45	0.256	2.26E+03	2.75E+03	1.11E+03	0.0517
(XY) - 135	0.2577	2.00E+03	2.87E+03	1.17E+03	0.0538
(YZ) - 90	0.0615	1.27E+04	642.5989	98.0306	0.0192
(YZ) - 45	0.2196	2.93E+03	1.62E+03	577.828	0.047
(YZ) - 135	0.2224	2.82E+03	1.64E+03	581.2431	0.0472
(XZ) - 45	0.1813	3.48E+03	1.43E+03	397.0102	0.041
(XZ) - 135	0.1959	2.89E+03	1.57E+03	522.4343	0.0467
Mean	**0.19902**	**4.27E+03**	**1.83E+03**	**633.5757**	**0.04252**

Table 6.4. GLRLM results for Exp.2. 1MHz - 0.1MPa

Exp.2 - low pressure - 1MHz					
Orientation	SRE.	LRE.	GLN.	RLN.	RP
(XY) - 0	0.2374	5.18E+03	2.28E+03	1.66E+03	0.0582
(XY) - 90	0.2197	6.58E+03	2.10E+03	1.39E+03	0.0538
(XY) - 45	0.2955	2.81E+03	3.00E+03	2.84E+03	0.0762
(XY) - 135	0.2955	2.93E+03	2.91E+03	2.55E+03	0.0733
(YZ) - 90	0.0518	1.53E+04	657.0725	182.7106	0.0261
(YZ) - 45	0.2055	5.98E+03	1.44E+03	752.7891	0.0617
(YZ) - 135	0.2279	5.20E+03	1.50E+03	822.1717	0.0647
(XZ) - 45	0.2744	1.74E+03	1.30E+03	866.8614	0.0662
(XZ) - 135	0.2761	1.64E+03	1.34E+03	912.2276	0.0686
Mean	**0.23153**	**5.26E+03**	**1.84E+03**	**1.33E+03**	**0.06098**

Table 6.5. GLRLM results for Exp.3. 1MHz - 0.3MPa

Exp.3 - High pressure - 1MHz					
Orientation	SRE.	LRE.	GLN.	RLN.	RP
(XY) - 0	0.2091	5.49E+03	1.73E+03	715.8204	0.0377
(XY) - 90	0.2247	5.38E+03	1.77E+03	778.7204	0.0385
(XY) - 45	0.2755	2.53E+03	2.40E+03	1.26E+03	0.051
(XY) - 135	0.2895	2.26E+03	2.50E+03	1.43E+03	0.0534
(YZ) - 90	0.0931	1.32E+04	733.2245	186.1354	0.0225
(YZ) - 45	0.228	4.25E+03	1.48E+03	666.972	0.0446
(YZ) - 135	0.2525	3.61E+03	1.62E+03	858.6143	0.0496
(XZ) - 45	0.219	5.16E+03	1.53E+03	654.3791	0.0457
(XZ) - 135	0.2262	5.45E+03	1.56E+03	731.7147	0.047
Mean	**0.22418**	**5.26E+03**	**1.70E+03**	**809.0951**	**0.04333**

Table 6.6. GLCM results for Exp.3. 1MHz - 0.1MPa

Exp.3 - Low pressure - 1MHz					
Orientation	SRE.	LRE.	GLN.	RLN.	RP
(XY) - 0	0.3299	7.10E+03	1.77E+03	1.72E+03	0.0531
(XY) - 90	0.3746	4.92E+03	2.03E+03	2.36E+03	0.061
(XY) - 45	0.403	2.95E+03	2.54E+03	3.27E+03	0.0742
(XY) - 135	0.4161	2.84E+03	2.60E+03	3.53E+03	0.0763
(YZ) - 90	0.1331	5.01E+03	568.1547	288.5073	0.0357
(YZ) - 45	0.3614	2.09E+03	1.12E+03	1.30E+03	0.0696
(YZ) - 135	0.3844	1.87E+03	1.21E+03	1.59E+03	0.0769
(XZ) - 45	0.231	1.14E+04	1.35E+03	1.15E+03	0.0657
(XZ) - 135	0.2379	1.11E+04	1.38E+03	1.22E+03	0.0675
Mean	**0.31904**	**5.48E+03**	**1.62E+03**	**1.83E+03**	**0.06444**

Table 6.7. GLRLM results for Exp.4. 2MHz - 0.1MPa

Exp.4 - Highe pressure - 2MHz					
Orientation	SRE.	LRE.	GLN.	RLN.	RP
(XY) - 0	0.2533	1.08E+04	1.29E+03	784.924	0.033
(XY) - 90	0.2696	8.41E+03	1.38E+03	952.1899	0.036
(XY) - 45	0.3148	4.39E+03	1.84E+03	1.43E+03	0.0459
(XY) - 135	0.3277	4.31E+03	1.92E+03	1.57E+03	0.0479
(YZ) - 90	0.1008	1.02E+04	723.5229	385.2596	0.0278
(YZ) - 45	0.3053	3.53E+03	1.35E+03	1.13E+03	0.0503
(YZ) - 135	0.2749	4.09E+03	1.25E+03	910.5132	0.0464
(XZ) - 45	0.2841	4.60E+03	1.24E+03	888.1834	0.0455
(XZ) - 135	0.293	3.98E+03	1.28E+03	918.7763	0.0463
Mean	**0.26928**	**6.03E+03**	**1.37E+03**	**997.194**	**0.04212**

Table 6.8. GLRLM results for Exp.4. 2MHz - 0.08MPa

Exp.4 - Low pressure - 2MHz					
Orientation	SRE.	LRE.	GLN.	RLN.	RP
(XY) - 0	0.3453	3.12E+03	2.69E+03	2.39E+03	0.0687
(XY) - 90	0.3505	3.28E+03	2.79E+03	2.51E+03	0.0702
(XY) - 45	0.386	1.73E+03	3.46E+03	3.47E+03	0.0849
(XY) - 135	0.4281	1.35E+03	3.80E+03	4.53E+03	0.0946
(YZ) - 90	0.0631	1.07E+04	873.3615	311.065	0.0314
(YZ) - 45	0.3198	3.31E+03	2.23E+03	2.03E+03	0.0786
(YZ) - 135	0.3299	2.88E+03	2.31E+03	2.11E+03	0.0811
(XZ) - 45	0.3549	1.23E+03	2.09E+03	2.03E+03	0.0795
(XZ) - 135	0.3441	1.18E+03	2.08E+03	1.87E+03	0.0772
Mean	**0.32463**	**3.20E+03**	**2.48E+03**	**2.36E+03**	**0.07402**

Table 6.9. GLRLM results for Exp.5. 2MHz - 0.1MPa

Exp.5 - High pressure - 2MHz					
Orientation	SRE.	LRE.	GLN.	RLN.	RP
(XY) - 0	0.2775	6.96E+03	1.64E+03	1.09E+03	0.0409
(XY) - 90	0.2733	5.83E+03	1.65E+03	1.05E+03	0.0406
(XY) - 45	0.3299	3.19E+03	2.20E+03	1.66E+03	0.0525
(XY) - 135	0.3635	2.65E+03	2.38E+03	2.11E+03	0.0576
(YZ) - 90	0.0772	1.57E+04	671.385	234.3658	0.0219
(YZ) - 45	0.2957	3.85E+03	1.63E+03	1.20E+03	0.0504
(YZ) - 135	0.2738	4.31E+03	1.50E+03	940.3501	0.0459
(XZ) - 45	0.3094	3.81E+03	1.61E+03	1.15E+03	0.049
(XZ) - 135	0.3058	3.91E+03	1.58E+03	1.12E+03	0.049
Mean	**0.27846**	**5.57E+03**	**1.65E+03**	**1.17E+03**	**0.04531**

Table 6.10. GLRLM results for Exp.5. 2MHz - 0.08MPa

Exp.5 - Low pressure - 2MHz					
Orientation	SRE.	LRE.	GLN.	RLN.	RP
(XY) - 0	0.3086	8.78E+03	1.76E+03	1.54E+03	0.0514
(XY) - 90	0.3817	6.47E+03	2.14E+03	2.65E+03	0.0645
(XY) - 45	0.391	3.66E+03	2.53E+03	3.19E+03	0.0744
(XY) - 135	0.4309	3.34E+03	2.80E+03	4.10E+03	0.0821
(YZ) - 90	0.1205	7.71E+03	898.6415	580.7023	0.0357
(YZ) - 45	0.4239	2.10E+03	2.04E+03	3.11E+03	0.0813
(YZ) - 135	0.3504	2.64E+03	1.73E+03	1.94E+03	0.0674
(XZ) - 45	0.3246	4.85E+03	1.96E+03	1.98E+03	0.0676
(XZ) - 135	0.3056	4.90E+03	1.89E+03	1.68E+03	0.0636
Mean	**0.33747**	**4.94E+03**	**1.97E+03**	**2.31E+03**	**0.06533**

Table 6.11. GLRLM results for averaged SHAM

SHAM - Average					
Orientation	SRE.	LRE.	GLN.	RLN.	RP
(XY) - 0	0.32782	9.20E+03	2458.08	1797.5	0.05346
(XY) - 90	0.34236	8696.18	2605.1	1956.24	0.05616
(XY) - 45	0.37988	4283.64	3460.58	2972.1	0.07148
(XY) - 135	0.38158	4225.72	3479.36	3009.02	0.072
(YZ) - 90	0.09742	9988.48	745.41524	240.5786	0.02576
(YZ) - 45	0.34278	2443.06	2031.32	1594.3	0.06456
(YZ) - 135	0.33806	2440.32	2036.38	1532.88	0.06388
(XZ) - 45	0.3264	1944.6	1954.74	1479.347	0.06242
(XZ) - 135	0.3202	2019.98	1923.54	1409.669	0.06122
Mean	**0.31739**	**5.03E+03**	**2.30E+03**	**1.78E+03**	**0.05899**

Table 7. Results obtained during the volumetric analysis, where tables 7.1 - 7.6 are the results for experiment 1,2, and 3, while tables 7.7 - 7.10 are for experiment 4 and 5. Table 7.11 is for averaged sham.

Table 7.1. Volumetric results for Exp.1. 1MHz - 0.3MPa

Exp.1 - High pressure - 1MHz	
Orientation	*Pixles*
(XY) - 0	21.1368
(XY) - 90	22.4485
(XY) - 45	15.7031
(XY) - 135	15.0604
(YZ) - 90	41.7824
(YZ) - 45	18.2372
(YZ) - 135	18.0696
(XZ) - 45	18.9129
(XZ) - 135	19.1233
% Volume	18.25

Table 7.2. Volumetric results for Exp.1. 1MHz - 0.1MPa

Exp.1 - Low pressure - 1MHz	
Orientation	*Pixles*
(XY) - 0	18.9277
(XY) - 90	16.8172
(XY) - 45	11.9076
(XY) - 135	13.2618
(YZ) - 90	51.3062
(YZ) - 45	17.473
(YZ) - 135	16.8228
(XZ) - 45	15.8074
(XZ) - 135	15.1676
% Volume	19.94

Table 7.3. Volumetric results for Exp.2. 1MHz - 0.3MPa

Exp.2 - High pressure - 1MHz	
Orientation	*Pixles*
(XY) - 0	25.7393
(XY) - 90	23.2175
(XY) - 45	17.3352
(XY) - 135	16.9776
(YZ) - 90	55.9386
(YZ) - 45	23.0077
(YZ) - 135	21.7019
(XZ) - 45	20.6005
(XZ) - 135	20.393
% Volume	20.42

Table 7.4. Volumetric results for Exp.2. 1MHz - 0.1MPa

Exp.2 - Low pressure - 1MHz	
Orientation	*Pixles*
(XY) - 0	30.4925
(XY) - 90	33.5559
(XY) - 45	21.6627
(XY) - 135	22.4728
(YZ) - 90	77.7944
(YZ) - 45	26.3677
(YZ) - 135	26.291
(XZ) - 45	29.3097
(XZ) - 135	27.7757
% Volume	27.86

Table 7.5. Volumetric results for Exp.3. 1MHz - 0.3MPa

Exp.3 - High pressure - 1MHz	
Orientation	*Pixles*
(XY) - 0	26.6024
(XY) - 90	25.4757
(XY) - 45	18.4714
(XY) - 135	18.2741
(YZ) - 90	48.5052
(YZ) - 45	22.5167
(YZ) - 135	22.3488
(XZ) - 45	22.3262
(XZ) - 135	21.0876
% Volume	19.32

Table 7.6. Volumetric results for Exp.3. 1MHz - 0.1MPa

Exp.3 - Low pressure - 1MHz	
Orientation	*Pixles*
(XY) - 0	23.7384
(XY) - 90	20.2542
(XY) - 45	15.4746
(XY) - 135	15.0547
(YZ) - 90	54.3366
(YZ) - 45	20.8629
(YZ) - 135	20.5398
(XZ) - 45	18.7622
(XZ) - 135	17.6123
% Volume	21.35

Table 7.7. Volumetric results for Exp.4. 2MHz - 0.1MPa

Exp.4 - High pressure - 2MHz	
Orientation	*Pixles*
(XY) - 0	26.638
(XY) - 90	25.5153
(XY) - 45	18.8382
(XY) - 135	17.9689
(YZ) - 90	46.8313
(YZ) - 45	22.344
(YZ) - 135	21.7345
(XZ) - 45	21.0303
(XZ) - 135	22.0405
% Volume	14.97

Table 7.8. Volumetric results for Exp.4. 2MHz - 0.08MPa

Exp.4 - Low pressure - 2MHz	
Orientation	*Pixles*
(XY) - 0	18.4519
(XY) - 90	16.9146
(XY) - 45	12.9795
(XY) - 135	12.1075
(YZ) - 90	56.3101
(YZ) - 45	17.0968
(YZ) - 135	17.0008
(XZ) - 45	16.1014
(XZ) - 135	15.4534
% Volume	22.35

Table 7.9. Volumetric results for Exp.5. 2MHz - 0.1MPa

Exp.5 - High pressure - 2MHz	
Orientation	*Pixles*
(XY) - 0	21.888
(XY) - 90	22.2101
(XY) - 45	16.2467
(XY) - 135	14.9806
(YZ) - 90	54.0219
(YZ) - 45	19.4147
(YZ) - 135	19.6621
(XZ) - 45	19.5532
(XZ) - 135	20.2155
% Volume	15.49

Table 7.10. Volumetric results for Exp.5. 2MHz - 0.08MPa

Exp.5 - Low pressure - 2MHz	
Orientation	*Pixles*
(XY) - 0	23.0025
(XY) - 90	20.1673
(XY) - 45	16.0287
(XY) - 135	14.3833
(YZ) - 90	50.7505
(YZ) - 45	19.9516
(YZ) - 135	20.3852
(XZ) - 45	17.4816
(XZ) - 135	19.0451
% Volume	20.72

Table 7.11. Volumetric results for averaged SHAM

SHAM-Avg	
Orientation	*Pixles*
(XY) - 0	12.72636
(XY) - 90	11.9908
(XY) - 45	8.70414
(XY) - 135	8.7624
(YZ) - 90	39.7808
(YZ) - 45	11.71306
(YZ) - 135	11.91068
(XZ) - 45	11.18594
(XZ) - 135	11.20414
% Volume	16.106

Appendix B

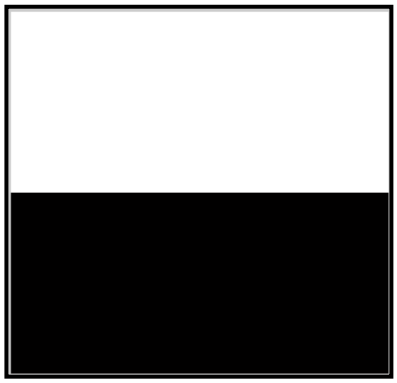

	TE	ENE	HOM	CON
XY - (0)	1	0.5	1	0
XY - (90)	1.037	0.4961	0.998	0.0039
XY - (45)	1.037	0.4961	0.998	0.0039
XY - (135)	1.037	0.4961	0.998	0.0039
MEAN	1.02775	0.497075	0.9985	0.002925

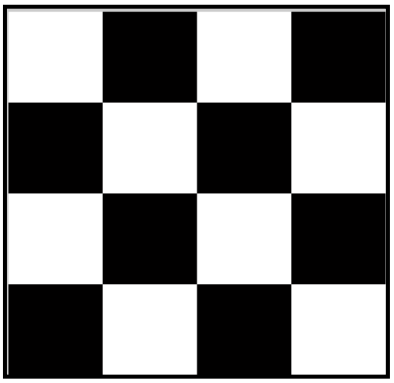

	TE	ENE	HOM	CON
XY - (0)	1.0923	0.4884	0.9941	0.0118
XY - (90)	1.0923	0.4884	0.9941	0.0118
XY - (45)	1.1593	0.4773	0.9883	0.0233
XY - (135)	1.1593	0.4773	0.9883	0.0233
MEAN	1.1258	0.48285	0.9912	0.01755

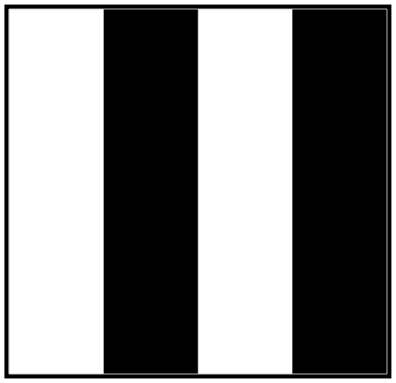

	TE	ENE	HOM	CON
XY - (0)	1.0923	0.4884	0.9941	0.0118
XY - (90)	1	0.5	1	0
XY - (45)	1.0923	0.4884	0.9941	0.0118
XY - (135)	1.0923	0.4884	0.9941	0.0118
MEAN	1.069225	0.4913	0.995575	0.00885

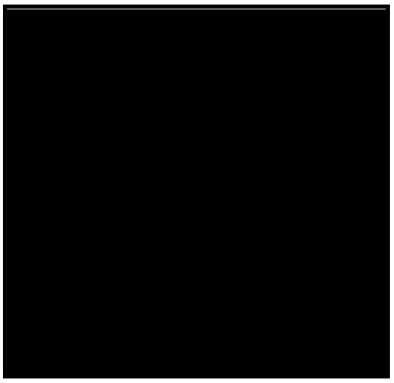

	TE	ENE	HOM	CON
XY - (0)	0	1	1	0
XY - (90)	0	1	1	0
XY - (45)	0	1	1	0
XY - (135)	0	1	1	0
MEAN	0	1	1	0

Figure. 16. The figure shows different intensity arrangements and their corresponding textural GLCM values.

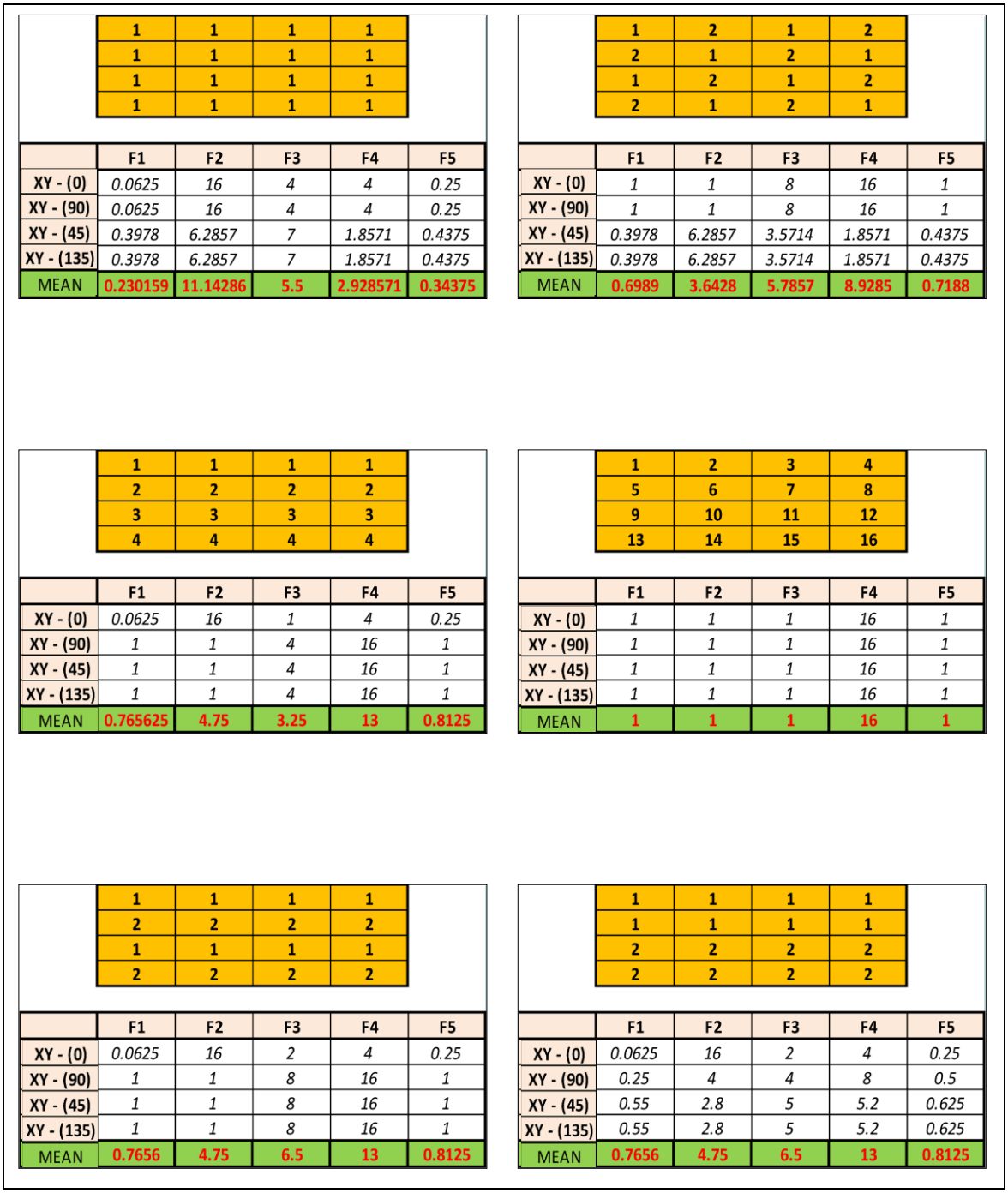

1	1	1	1
1	1	1	1
1	1	1	1
1	1	1	1

	F1	F2	F3	F4	F5
XY - (0)	0.0625	16	4	4	0.25
XY - (90)	0.0625	16	4	4	0.25
XY - (45)	0.3978	6.2857	7	1.8571	0.4375
XY - (135)	0.3978	6.2857	7	1.8571	0.4375
MEAN	0.230159	11.14286	5.5	2.928571	0.34375

1	2	1	2
2	1	2	1
1	2	1	2
2	1	2	1

	F1	F2	F3	F4	F5
XY - (0)	1	1	8	16	1
XY - (90)	1	1	8	16	1
XY - (45)	0.3978	6.2857	3.5714	1.8571	0.4375
XY - (135)	0.3978	6.2857	3.5714	1.8571	0.4375
MEAN	0.6989	3.6428	5.7857	8.9285	0.7188

1	1	1	1
2	2	2	2
3	3	3	3
4	4	4	4

	F1	F2	F3	F4	F5
XY - (0)	0.0625	16	1	4	0.25
XY - (90)	1	1	4	16	1
XY - (45)	1	1	4	16	1
XY - (135)	1	1	4	16	1
MEAN	0.765625	4.75	3.25	13	0.8125

1	2	3	4
5	6	7	8
9	10	11	12
13	14	15	16

	F1	F2	F3	F4	F5
XY - (0)	1	1	1	16	1
XY - (90)	1	1	1	16	1
XY - (45)	1	1	1	16	1
XY - (135)	1	1	1	16	1
MEAN	1	1	1	16	1

1	1	1	1
2	2	2	2
1	1	1	1
2	2	2	2

	F1	F2	F3	F4	F5
XY - (0)	0.0625	16	2	4	0.25
XY - (90)	1	1	8	16	1
XY - (45)	1	1	8	16	1
XY - (135)	1	1	8	16	1
MEAN	0.7656	4.75	6.5	13	0.8125

1	1	1	1
1	1	1	1
2	2	2	2
2	2	2	2

	F1	F2	F3	F4	F5
XY - (0)	0.0625	16	2	4	0.25
XY - (90)	0.25	4	4	8	0.5
XY - (45)	0.55	2.8	5	5.2	0.625
XY - (135)	0.55	2.8	5	5.2	0.625
MEAN	0.7656	4.75	6.5	13	0.8125

Figure. 17. The figure shows different intensity arrangements and their corresponding GLRLM textural values.

Appendix B

MATVTK setup instructions:

- ***Windows 32-bit is preferred*** (the following instruction are on win-64).
- ***MATLAB 32-bit is needed.***
- ***Visual Studio Express 32-bit is needed.***

1. how to obtain the VTK Visualization Tool Kit (www.vtk.org) source code.

a) Download the VTK source code (not the .exe file) vtk-5.10.0 zip from **http://www.vtk.org/get-software.php**

b) Unzip the code in C:\Program Files (x86)\VTK 5.10\VTK.

c) Optionally, download example data files vtkdata-5.10.0 zip.

d) Optionally, Unzip this into the directory C:\Program Files\VTK 5.10 \VTKData. (Further steps are not included in this instruction)

2. Compile VTK to shared libraries

a) Download CMake utility from http://www.cmake.org/HTML/Download.html

"CMake is a utility that is used for compiling VTK on various platforms."

b) Unzip CMake in C:\Program Files (x86)\CMake 2.8

c) Run CMake (C:\Program Files (x86)\CMake 2.8\bin\CMakeSetup.exe).

d) In the "Where is the source code" dialog put C:\Program Files (x86)\VTK 5.10\VTK.

e) Create the directory C:\Program Files (x86)\VTK 5.10\Build

f) Put the directory from (e) into the "Where to build the binaries" dialog.

g) Set BUILD_SHARED_LIBS to ON

h) Set VTK_USE_MATLAB_MEX to ON

i) Press the Configure button to save the setting changes, then press it again.

j) Press Generate button to create various utilities that are used for building the VTK libraries (Will be found in C:\Program Files (x86)\VTK 5.10\Build).

k) Start Visual Studio and load the project that was created by CMake located in C:\Program Files\VTK 5.0\Build\VTK.sln

l) Build the project (Select ALL_BUILD), then the libraries will be created in C:\Program Files\VTK 5.0\Build\bin\debug

m) Put the generated libraries path from the build on the System path and on MATLAB path, so that they can be called from MATLAB.

3. Installing VTK (Yes! not Installed yet. It will be in (C:/Program Files (x86)/VTK) not VTK-5.8.0)

a) Run CMake (C:\Program Files (x86)\CMake 2.8\bin\CMakeSetup.exe).

b) In the "Where is the source code" dialog put C:\Program Files (x86)\VTK 5.10\VTK.

c) Create the directory C:\Program Files (x86)\VTK

d) Put the directory from (c) into the "Where to build the binaries" dialog.

e) Set BUILD_SHARED_LIBS to ON

f) Set VTK_USE_MATLAB_MEX to ON

h) Press the Configure button to save the setting changes, then press it again.

i) Press Generate button.

j) Start Visual Studio and load the project that was created by CMake located in C:\Program Files\VTK\VTK.sln

k) Build the project (Select ALL_BUILD), then the libraries will be created in C:\Program Files (x86)\VTK This will be so fast.

l) Select the "INSTALL" target, then press right click on it and choose "Build this target only". Now you VTK is ready.

m) Put the generated libraries path from the build on the System path and on MATLAB path, so that they can be called from MATLAB.

3. Download MATVTK

a) Download ***matVTK 1.0 beta1*** from http://www.cir.meduniwien.ac.at/matvtk/

b) Extract the files anywhere you want.

c) Open DEMO.M file in MATLAB and run the code. It should generate a 3D volume (make sure to choose the right path).